ORIGINAL PAPER

Microstructural evolution of silicate immiscible liquids in ferrobasalts

Victoria C. Honour[1] · Marian B. Holness[1] · Jamie L. Partridge[2] · Bernard Charlier[3]

Abstract

An experimental study of the microstructural evolution of an immiscible basaltic emulsion shows that the Fe-rich liquid forms homogeneously nucleated droplets dispersed in a continuous Si-rich liquid, together with droplets heterogeneously nucleated on plagioclase, magnetite, and pyroxene. Heterogeneous nucleation is likely promoted by localised compositional heterogeneities around growing crystals. The wetting angle of Fe-rich droplets on both plagioclase and magnetite increases with decreasing temperature. Droplet coarsening occurs by a combination of diffusion-controlled growth and Ostwald ripening, with an insignificant contribution from coalescence. Characteristic microstructures resulting from the interaction of immiscible Fe-rich liquid with crystal grains during crystal growth can potentially be used as an indicator of liquid unmixing in fully crystallised natural samples. In magma bodies $< \sim 10$ m in size, gravitationally driven segregation of immiscible Fe-rich droplets is unlikely to be significant.

Keywords Immiscibility · Nucleation kinetics · Droplet size distributions · Wetting angle · Ferrobasalt · Binodal

Introduction

Co-existing Fe- and Si-rich melt inclusions (e.g., Fischer et al. 2016; Jakobsen et al. 2005, 2011; Luais 1987; Roedder and Weiblen 1970) and Fe-rich droplets dispersed in Si-rich glassy mesostasis in rapidly cooled natural examples (e.g., De 1974; Philpotts 1982; Philpotts and Doyle 1980) provide evidence of immiscibility in ferrobasaltic liquid. The physical behaviour of these immiscible liquids in a crystal mush may play an important role in the evolution of mafic intrusions, particularly if there is relative movement of the two liquids (e.g., Holness et al. 2011; VanTongeren and Mathez 2012; Zhou et al. 2013).

✉ Victoria C. Honour
    vch28@cam.ac.uk

1   Department of Earth Sciences, University of Cambridge, Cambridge CB2 3EQ, UK

2   Department of Applied Mathematics and Theoretical Physics, Cambridge CB3 0WA, UK

3   Department of Geology, University of Liège, Sart Tilman, Liège, Belgium

Published experimental work on liquid immiscibility in ferrobasalts has primarily assessed the conditions (e.g., temperature, pressure, composition, fO_2) under which unmixing occurs, evolving in experimental complexity from five-component systems (e.g., Naslund 1976; Visser and Koster Van Groos 1976) to complex multiphase systems that more closely replicate basaltic liquids (e.g., Charlier and Grove 2012; Hou et al. 2017, 2018; Hou and Veksler 2015; Veksler et al. 2008). There is little corresponding work on the microstructural evolution of systems containing immiscible liquids, despite its importance in controlling mass transport and large-scale chemical fractionation.

Veksler et al. (2010) measured the interfacial tension between co-existing Fe-rich and Si-rich unmixed liquids and showed that, as expected, it increases with decreasing temperature as the liquids become more dissimilar in composition. The unmixed liquids in experimental charges are observed to separate with either sharp or diffuse interfaces (Charlier and Grove 2012; Dixon and Rutherford 1979; Hou and Veksler 2015; Longhi 1990; Philpotts and Doyle 1983; Veksler et al. 2008). The diffuse interfaces have been attributed to slow chemical diffusion (Hou and Veksler 2015). Cooling rate affects the size of the immiscible Fe-rich droplets and the extent of coarsening (Martin and Kushiro 1991). The differential flow of the two immiscible liquids in a porous medium, driven by density differences, has been

investigated in fluid dynamical models (Dufek 2016; Hassanizadeh 2016), but these models do not account for any control on liquid migration through a crystal mush by the effect of emulsion coarsening, or different wetting properties of the two liquids [about which little is known, despite the importance of wetting angle in sintering and grain boundary formation (German et al. 2009)].

What is currently missing is a systematic, quantitative study of the kinetics of unmixing and microstructural evolution of immiscible liquids in basaltic systems. Here, we report the results of an experimental study designed to address this gap in our understanding and for comparison with natural samples. We conducted anhydrous one-atmosphere crystallisation experiments on ferrobasaltic compositions, in which unmixing is manifested by the separation of Fe-rich droplets in a continuous Si-rich phase, and analysed the resultant microstructures to provide insights into the processes controlling the physical behaviour of unmixing and coarsening of immiscible liquids in a crystal mush. Using backscatter electron images on 2D slices through the experimental charges, we quantify the wetting angles of Fe-rich droplets on crystal phases, produce droplet size distributions (DSDs), and link these textural characteristics to the spatial distribution and composition of the Fe-rich droplets.

Experimental methods and analytical procedures

Starting materials

We chose a sample of monzonitic composition from the Sept Iles Intrusion (Quebec, Canada), sample 03-41, that has been studied by Namur et al. (2011) and Charlier and Grove (2012) (Table 1). The sample originally contained 165 ppm Ce, 103 ppm Y and 786 ppm Zr. We doped the starting composition to reach 1000 ppm for these elements and also for Rb; the former three elements preferentially partition into an immiscible Fe-rich liquid, whereas the latter preferentially partitions into an immiscible Si-rich liquid (Veksler et al. 2006).

Data obtained from microstructural analysis of seven experimental charges produced by Charlier and Grove (2012) are also presented in this study. These charges have starting compositions of sample 03-41 from the Sept Iles Intrusion (Canada; experiments: SI-5, SI-8, SI-9) and an intermediate basalt from the Mull Tertiary volcano (Scotland; experiments: M-9, M-5, M-6, M-7; Table 1). Both localities preserve evidence of immiscibility (Charlier et al. 2011; Namur et al. 2012; Philpotts 1982).

Experimental techniques

Anhydrous one-atmosphere experiments were performed using a GERO HTRV 70-250/18 vertical tube furnace at the University of Liège, Belgium. The starting materials were suspended in the hot spot of the furnace (ca. 5 cm with a temperature within ± 1 °C). The sample temperature was measured using a $Pt–Pt_{90}Rh_{10}$ thermocouple calibrated to the melting points of Ag and Au. The experimental charge was prepared on a 0.2 mm iron–platinum alloy loop, which had been previously annealed with 11 wt% Fe added by electroplating to prevent Fe loss to the alloy during the experiment (Grove 1981). The oxygen fugacity in the alumina tube was controlled using mixtures of high-purity CO and CO_2 flushed from bottom to top. Bronkhorst gas flow controllers were used to control the flow rate at 0.12 cm/s. The furnace tube, the water-cooled flange, and the gas connections

Table 1 Compositions of starting materials (wt%) (Charlier and Grove 2012; Philpotts and Philpotts 2005)

	Sept Iles	Mull	Kilauea Iki lava lake	Cohasset flood-basalt flow
No. of analyses	15	17 (Charlier and Grove 2012)	45	Whole rock XRF (Philpotts and Philpotts 2005)
SiO_2	57.91	54.9	54.22	53.4
TiO_2	2.07	2.40	3.99	1.67
Al_2O_3	14.78	13.40	12.55	13.81
FeO	10.57	14.40	11.88	11.7
MnO	0.09	0.19	0.19	0.2
MgO	2.16	3.35	3.62	5.2
CaO	4.69	6.36	6.94	8.9
Na_2O	4.51	2.31	2.87	2.6
K_2O	2.64	1.45	1.60	1.2
P_2O_5	0.78	0.92	0.91	0.2
Total	100.20	99.68	98.78	98.88
Mg#	26.5	29.0	21.5	28.6

form a gas-tight system. The oxygen fugacity was monitored using a zirconium dioxide oxygen sensor and was kept at the QFM buffer. Prior to experiments, some sample pellets were heated to 1104 °C at QFM, while others were heated in a muffle furnace in air to 1150 °C (see later for implications), but both sets were quenched in air.

The experimental run conditions are detailed in Table 2. Nine experimental charges were cooled at 1 °C/h to different temperatures and quenched in water (Fig. 1). Pre-quench temperatures of the experimental charges ranged from 1150 to 955 °C. An additional six samples were cooled at 1 °C/h and then held isothermally at 1021 or 1000 °C for up to 158 h or 182 h, respectively. These experiments, which we describe as "isothermal" for simplicity, were quenched in water after different dwell times (at 1021 °C: $t_{12} = 12$ h, $t_{40} = 40$ h, $t_{158} = 158$ h; at 1000 °C: $t_{18} = 18$ h, $t_{62} = 62$ h, $t_{182} = 182$ h). Experiments were held at 1100 °C prior to cooling to ensure equilibration at QFM. Unless described as experimental charges that were subjected to an isothermal dwell time, the temperatures used to describe the experimental charges are the pre-quench temperatures, after 1 °C/h cooling with no time spent isothermally.

Natural samples

We chose two well-characterised natural examples of liquid immiscibility for preliminary microstructural comparisons with the experiments, based on their similarities in composition and temperature history to the experiments (Table 1):
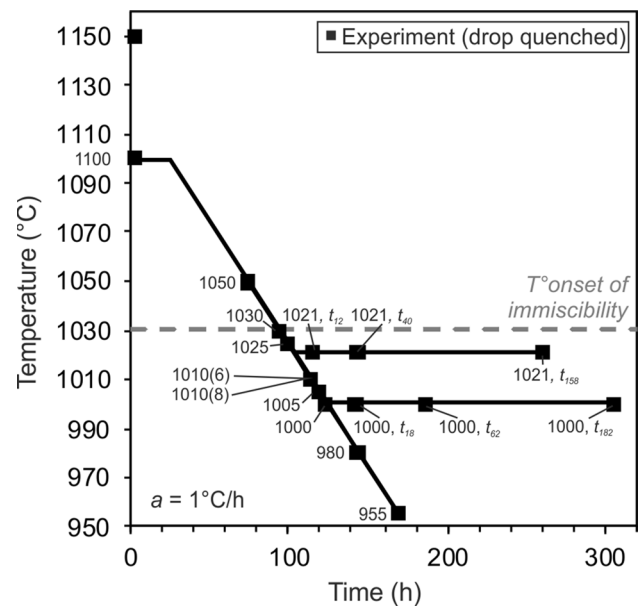
Fig. 1 Temperature–time paths for experimental runs with a constant cooling rate (Table 2). There is a variable duration along a final isothermal plateau for two different experiments held at different temperatures (1000 °C and 1021 °C). The duration (in hours; Z) that each experiment was held at for that temperature is indicated by t_Z. $a =$ the cooling rate of the experiments

(1) the 1976 drill core from the Kilauea Iki lava lake in Hawaii, USA (e.g., Helz 1980); and (2) the Cohasset flood-basalt flow, Hanford, Washington, USA (e.g., Philpotts and Philpotts 2005).

Table 2 Experimental conditions and phases present

| Run	Starting temperature (°C)	Final temperature (°C)	Time (h)	Cooling method	Starting preparation	Phases present
VIC08	1100	1050	74	1 °C/h	Melted to 1150 °C: muffle furnace	gl, pl, aug, pig, mt
VIC06	1100	*1030*	94	1 °C/h	Melted to 1104 °C @ QFM	gl Si, gl Fe, pl, ol, aug, pig, tmt, mt
VIC08	1100	1025	99	1 °C/h	Melted to 1150 °C: muffle furnace	gl Si, gl Fe, pl, aug, pig, mt, wht
VIC08	1100	1010	114	1 °C/h	Melted to 1150 °C: muffle furnace	gl Si, gl Fe, pl, aug, pig, mt, wht
VIC06	1100	*1010*	114	1 °C/h	Melted to 1104 °C @ QFM	gl Si, gl Fe, pl, ol, aug, pig, mt, wht
VIC07	1100	1005	119	1 °C/h	Melted to 1150 °C: muffle furnace	gl Si, gl Fe, pl, aug, pig, mt, wht
VIC09	1100	1000	124	1 °C/h	Melted to 1150 °C: muffle furnace	gl Si, gl Fe, pl, aug, mt, wht
VIC09	1100	980	144	1 °C/h	Melted to 1150 °C: muffle furnace	gl Si, gl Fe, pl, aug, pig, mt, wht
VIC09	1100	955	169	1 °C/h	Melted to 1150 °C: muffle furnace	gl Si, gl Fe, pl, aug, pig, mt, wht
VIC10	1100	1021	115	Isothermal	Melted to 1150 °C: muffle furnace	gl Si, gl Fe, pl, aug, pig, mt. wht
VIC10	1100	1021	143	Isothermal	Melted to 1150 °C: muffle furnace	gl Si, gl Fe, pl, aug, pig, mt, wht
VIC10	1100	1021	261	Isothermal	Melted to 1150 °C: muffle furnace	gl Si, gl Fe, pl, aug, pig, mt, wht
VIC06	1100	*1000*	142	Isothermal	Melted to 1104 °C @ QFM	gl Si, gl Fe, pl, ol, aug, pig, mt, wht
VIC07	1100	1000	186	Isothermal	Melted to 1150 °C: muffle furnace	gl Si, gl Fe, pl, aug, pig, mt, wht
VIC07	1100	1000	306	Isothermal	Melted to 1150 °C: muffle furnace	gl Si, gl Fe, pl, aug, pig, mt, wht

Italicised final temperature values denote experiments prepared @ QFM

gl glass, *pl* plagioclase, *ol* olivine, *aug* augite, *pig* pigeonite, *il* ilmenite, *tmt* titanomagnetite, *mt* magnetite, *wht* whitlockite

Analyses

The experimental charges were split and mounted in epoxy. The charges were analysed using a Quanta FEG 650 F SEM at the Department of Earth Sciences, University of Cambridge, using a 10 kV beam at spot 3, with a 30 μm aperture and a working distance of 10 mm. This provided semi-quantitative mineral compositions, element energy-dispersive X-ray spectroscopy (EDS) maps and backscatter electron (BSE) imagery (Fig. 2a–d). Images (3072 × 2048 pixels in size) were collected from transects across each experiment, with a dwell time of 20 μs.

The area of each Fe-rich droplet, and the number of droplets, were quantified from BSE images using *Matlab R2017b*. The smallest effective droplet diameter that could be resolved for image analysis was 0.25 μm. There are two types of Fe-rich droplet: attached droplets are in contact with a crystal phase, whereas isolated droplets are (at least in the 2D plane of the image) surrounded by glass (Fig. 2e–f). We measured attached droplets and isolated droplets separately. The effective diameters of all Fe-rich droplets (as viewed in 2D) were calculated from their area, assuming a circular shape. The true, 3D, distribution of droplet sizes was calculated using *CSDCorrections1.6* (Higgins 2000), assuming
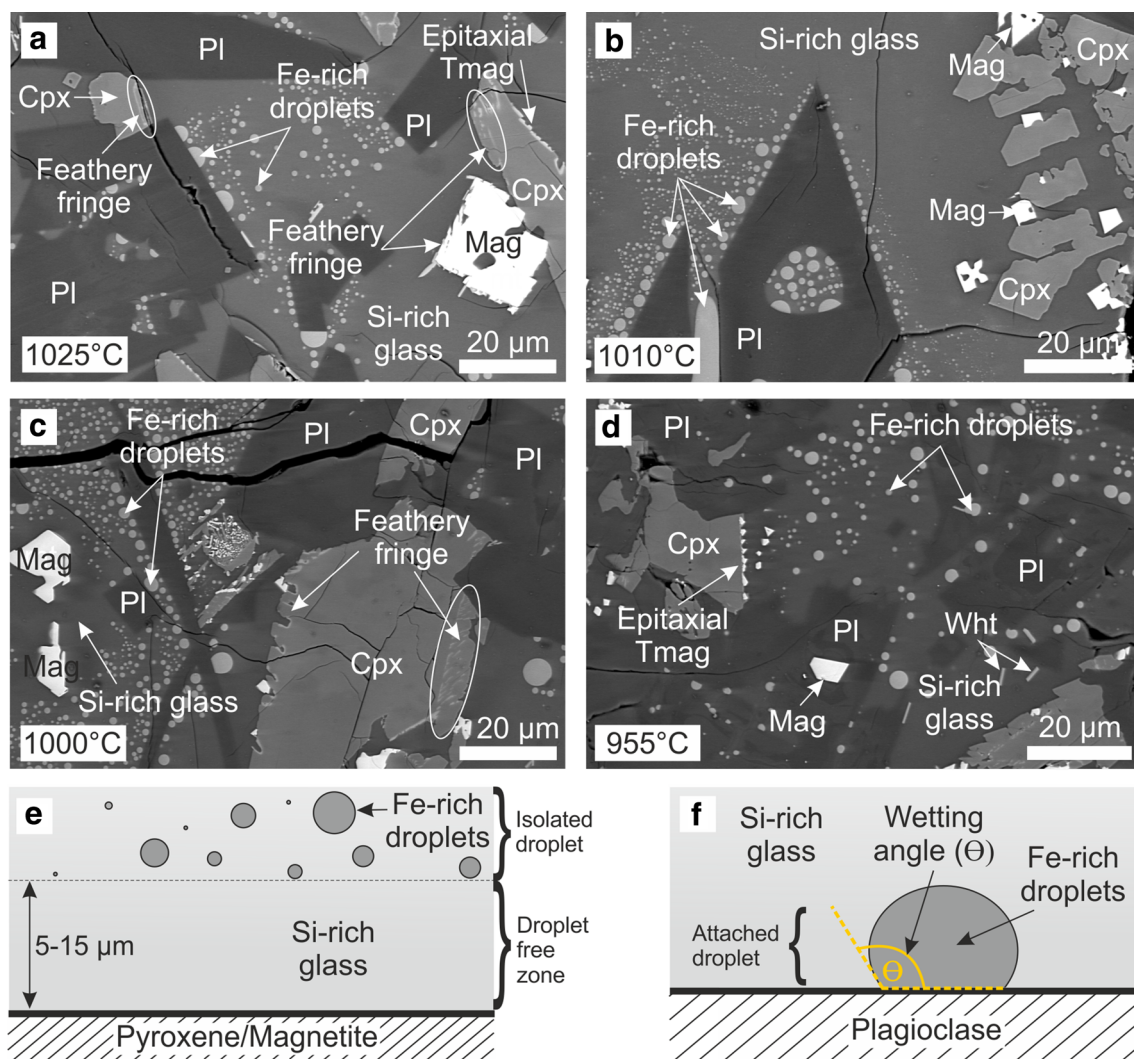
Fig. 2 Backscatter electron (BSE) images of the experimental charges at different temperatures with constant cooling of 1 °C/h. **a** Fe-rich droplets, at 1025 °C, are attached to plagioclase and isolated in the interstitial Si-rich glass. Note the feathery fringes on the pyroxene and magnetite. **b** Fe-rich droplets at 1010 °C, with bigger attached droplets than isolated droplets. The isolated droplets preferentially surround the plagioclase grains, avoiding the mafic phases. **c** Immis-cibility at 1000 °C with Fe-rich droplets situated close to plagioclase, and a droplet-free zone around pyroxene and magnetite. **d** The Fe-rich droplets are uniformly distributed at 955 °C. **e** A cartoon depicting the difference in size and frequency of attached versus isolated Fe-rich droplets. **f** A cartoon illustrating the apparent wetting angle of an Fe-rich droplet on a crystal face. Mineral abbreviations after Whitney and Evans (2010)

a spherical shape and using a logarithmic base 2 scale to calculate bin sizes.

The wetting angle of Fe-rich droplets in contact with plagioclase, magnetite and pyroxene was determined from populations of > 20 apparent wetting angles per experimental charge, using BSE images using *CorelDRAW X7* to measure the angle from the crystal surface through the Fe-rich droplet (Fig. 2f) (Mungall and Su 2005; Rotenberg et al. 1983). Measurements were taken for both sides of each droplet, and all discernible attached droplets in each image were measured. The median of a population of at least 25 measurements of apparent (2D) angles is within a few degrees of the true (3D) angle (Riegger and Van Vlack 1960). We determined the 95% confidence intervals for the true (3D) angle according to the method of Wilks (1962) as reported by Stickels and Hucke (1964).

Following the methodology outlined by Holness (2014), the 'fit ellipse' function in *ImageJ* software was used to calculate plagioclase apparent aspect ratios from measurements of the long and short axes of a minimum of 250 plagioclase grains per sample, from BSE images. In each image, all discernible plagioclase grains were measured. We use the parameter AR, defined as the average apparent aspect ratio of plagioclase as viewed in thin section (e.g., Boorman et al. 2004; Holness et al. 2017); this can be used as a measure of grain shape with no associated assumptions about the range of 3D shapes (c.f. Higgins 1994), and changes systematically with cooling rate (Holness 2014). The 95% confidence intervals for AR were calculated using bootstrap sampling. Average apparent plagioclase grain sizes were quantified using the long axis of a minimum of 250 plagioclase grains, for which the length was determined using the perimeter function in *ImageJ* software.

Mineral and glass compositions were measured using a Cameca SX-100 electron microprobe with five WDS spectrometers at the Department of Earth Sciences, University of Cambridge. The instrument uses PeakSight software with ZAF correction. Appropriate natural and synthetic primary standards were used. The glass analyses were run at 15 kV, 4 nA with a defocused 10 μm, 5 μm and 2 μm beam. Regardless of the beam size, 40 analyses of natural and synthetic glasses (Basalt glass Makaopuhi Lava Lake HI NMNH 113498-1 A-99; and Corning Glass Reference 'D' NMNH 117218-3) had standard deviations of 0.5 wt% or less for all elements (S. Table A). Na and Si were analysed on peak for 10 s; Al for 20 s; K, Ca, Mg and Fe for 30 s; Mn and Ti for 40 s, and P, Y, Zr and Ce for 60 s. Mineral compositions were analysed at 15 kV, 10 nA with a focused beam; Na and Si were analysed for 10 s on peak, Al for 20 s, Ca, Mg, K, Ti and Mn for 30 s, and Fe for 40 s. Relevant mineral and glass secondary standards were run at regular intervals to check for precision and reproducibility. The experimental phase composition analyses generally had standard deviations below 1 wt%. Analyses were normalised to an internal standard (Basalt glass Makaopuhi Lava Lake HI NMNH 113498-1 A-99 and fayalite, Rockport, NMNH 85276) for consistency between runs. The mineral phases were analysed on their rims. Analyses of Fe-rich immiscible droplets were challenging due to the typically small area presented (< 25 μm^2), together with the unknown 3D droplet shape creating uncertainty about the electron beam interaction volume [this was modelled using *Casino v2.48* software (Drouin et al. 2007)]. Hence, while each droplet was analysed in its apparent centre, there may have been a component of mixing with the surrounding Si-rich conjugate.

Electron backscatter diffraction (EBSD) data were collected to obtain crystallographic orientations of pyroxene, titanomagnetite and whitlockite, at the Department of Earth Sciences, University of Cambridge, using a Quanta FEG 650 F SEM. Data collection, indexing, analysis of electron backscatter diffraction patterns, EBSD maps and pole figures were processed by *Bruker Esprit 2.1* software and the MTEX Toolbox run in *Matlab R2017b*.

Results

Phase composition

Glass, plagioclase, augite and pigeonite are the major phases in each experimental charge, with accessory magnetite, whitlockite (a calcium phosphate) and rare dendritic ilmenite and olivine (Table 2). Phase compositions are presented in the S. Table B. At 1030 °C and below, the glass comprises Fe-rich droplets dispersed within a continuous Si-rich phase (Fig. 2). Due to volatile loss in our anhydrous one-atmosphere experiments, whitlockite crystallises instead of apatite, with a similar arrival point on the liquidus (Tollari et al. 2006). At a constant cooling rate of 1 °C/h, and with no isothermal dwell time, the volume of the solid fraction increases with decreasing temperature: for example, the experimental charge quenched at 955 °C has a solid fraction of 57% (in 2D cross-section).

Given a constant cooling rate of 1 °C/h, plagioclase An# (mol.%) evolves from An_{48} at a temperature of 1100 °C to An_{29} at 955 °C; the plagioclase grains are normally zoned. In the same temperature interval, the Mg# (mol.%) of augite and pigeonite decreases from 46 to 42 and from 56 to 54, respectively. In the experiments in which olivine is present (Table 2), the forsterite number (mol.%) was 49 at 1030 °C, decreasing to 48 at 1010 °C and 43 at 1000 °C after 18 h dwell time at 1000 °C (t_{18}).

The "isothermal" experiments were cooled at a constant rate of 1 °C/h, and then held at 1021 °C and 1000 °C for 158 h and 182 h, respectively. The experimental charges contain glass, plagioclase, augite and pigeonite as the major

phases, with accessory magnetite and whitlockite. Olivine is present in the experimental charge t_{18} at 1000 °C. Bulk crystallinity (with the solid component dominated by plagioclase) increases with isothermal dwell time, and with decreasing isothermal dwell temperature: from 28% at 1021 °C t_{12} to 32% at t_{158}; and from 30% at 1000 °C t_{18} to 37% at t_{182}. The average plagioclase An# (mol.%) decreases as isothermal dwell time increases: at 1021 °C from An_{37} at t_{12}, to An_{35} at t_{158}, and at 1000 °C from An_{40} at t_{18}, to An_{37} at t_{182}. Augite Mg# decreases with increased dwell time.

Microstructure

The silicate liquid immiscibility binodal

The term 'binodal' describes the field of liquid immiscibility—the region on a phase diagram below which it is energetically favourable for a single liquid phase to unmix. Unmixing of a cooling liquid commonly occurs simultaneously with crystal growth and can occur by nucleation of droplets of the volumetrically minor phase. Such nucleation is limited by thermodynamic and kinetic barriers. Alternatively, unmixing can occur by spontaneous spinodal decomposition if the liquid experiences a large, (near-) instantaneous undercooling (Cahn 1961). There are no thermodynamic barriers to spinodal decomposition; however, there will be kinetic limitations. The typical microstructure indicative of spinodal decomposition is "a highly inter-connected fat spaghetti-like structure which contrasts with the separated growing blobs associated with nucleation and growth" (Elliott 1989).

Immiscible liquids

In the experimental charge quenched at 1030 °C, Fe-rich droplets are concentrated in the interstices of skeletal plagioclase. In the experimental charges quenched at, or below 1025 °C, Fe-rich droplets are widely distributed (Fig. 2a), either isolated in the continuous Si-rich glass, or attached to crystal surfaces. Fe-rich droplets preferentially attach to plagioclase, but at temperatures < 1005 °C they are also commonly attached to magnetite and pyroxene.

A single plagioclase face can have many attached Fe-rich droplets, ranging in diameter from sub-micron to 10 μm (as measured in 2D). The number and/or size of the attached Fe-rich droplets do not correlate with plagioclase grain size; however, crystal faces with large attached droplets (> 6 μm diameter) tend to be associated with fewer, small, attached droplets. Close to the top of the binodal (e.g., 1025 °C), single large Fe-rich droplets are commonly attached to the fastest growth faces of the plagioclase [i.e., those faces perpendicular to (010)]. At lower temperatures (1010 °C to 955 °C), the Fe-rich droplets show no consistent preference for any particular crystal face, regardless of the nature of the substrate. Mafic crystals rarely have multiple attached droplets. Instead, the crystal faces may be covered by a single droplet with a low apparent wetting angle.

Isolated Fe-rich droplets vary from sub-micron to 10 μm in diameter (viewed in 2D). Rare examples of droplet coalescence are preserved (Fig. 3). Isolated droplets in experimental charges run at temperatures < 1005 °C are larger on average than attached droplets. The spatial distribution of isolated droplets in the experimental charges is highly heterogeneous, with large droplet-free volumes (> 20 μm² in 2D), contrasting with abundant droplets in semi-enclosed regions surrounded by plagioclase (Fig. 2b). A 5–15 μm wide Fe-rich droplet-free zone often surrounds pyroxene, oxide and whitlockite. Furthermore, there is commonly a 2–4 μm wide droplet-free boundary zone between droplets attached to plagioclase grains and droplets isolated in the surrounding Si-rich glass (Fig. 2b). The Fe-rich droplets become more uniformly dispersed in the Si-rich glass with longer isothermal dwell times.

Pyroxene

The pyroxene grains display two main features (Fig. 2): (1) epitaxial growth of titanomagnetite on planar faces, observed at 1050 °C and below; and (2) feathery fringes, 1–3 μm wide, observed at 1025 °C and below. These feathery fringes comprise a marginal growth structure of crystalline, approximately oval, inclusions along the margins of the pyroxene grains, defining the euhedral core of the grain, and generally with a consistent shape orientation. They are found on any crystal face and are comprised chiefly of a mineral phase dominated by P and Ca, with a crystalline diffraction pattern most consistent with that of whitlockite. The whitlockite has a preferred orientation relationship with respect to each augite crystal face; however, this does not appear to consistently correlate with particular crystal faces of either whitlockite or augite. Features (1) and (2) are found on the same grain, but never on the same crystal face (Fig. 2c). Hammer et al. (2010) report a similar epitaxial relationship between clinopyroxene and titanomagnetite, with one of the symmetrically equivalent {110} faces of titanomagnetite aligned with the clinopyroxene (010) face. The clinopyroxene–titanomagnetite epitaxial relationship and the feathery fringes are also visible in natural samples from the Cohasset lava flow, USA (Fig. 4a).

Plagioclase

In experimental charges quenched at 1010 °C and 1000 °C, plagioclase laths develop pillar structures along crystal faces perpendicular to [001] that protrude 2–5 μm outward into the surrounding glass (the interstitial glass is > 45 modal % of
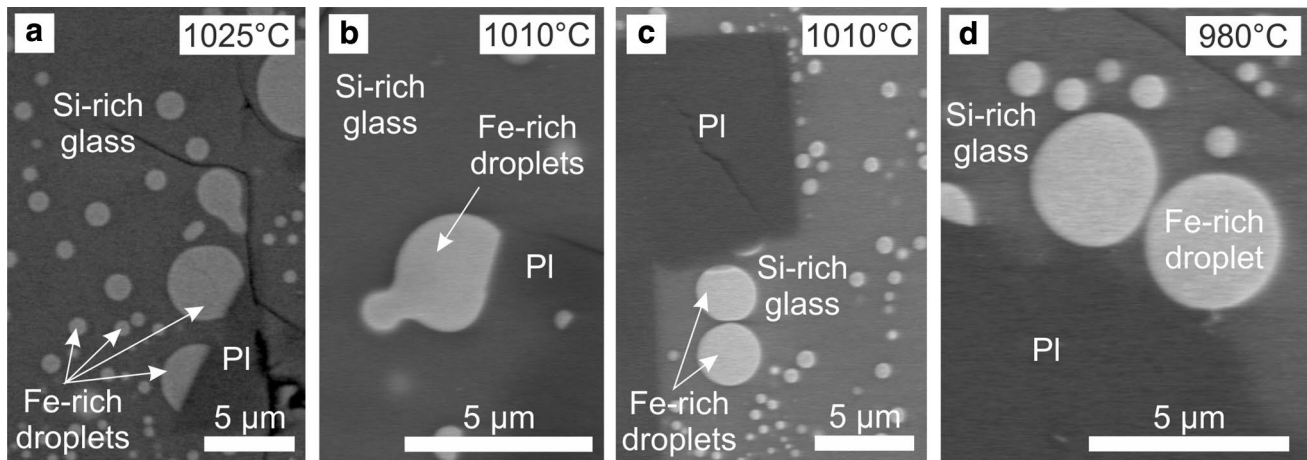
Fig. 3 Fe-rich droplet coalescence (**a**) and (**b**); near droplet coalescence (**c**) and (**d**)

the experimental charge). The pillars [first described by Philpotts (1981)] are 3–7 μm wide, and are each enclosed by an attached Fe-rich droplet of slightly larger diameter (Fig. 4b). Several pillars may be present on a single plagioclase crystal face, giving a crenulated appearance to the plagioclase edge, analogous to medieval castle battlements. Plagioclase pillars are also present in samples from the entablature of the Cohasset lava flow, USA (Fig. 4c), and in the upper crust of the Kilauea Iki lava lake, Hawaii, USA (Fig. 4d). In the Kilauea Iki samples, the pillars are observed in samples quenched (by water during drilling) at 1017 °C; this is comparable to the temperature of the experimental charges showing this microstructure. In our experimental charges and the natural samples, the pillars are more albitic than the substrate plagioclase (Fig. 4d') and the contact between the two compositional regions is sharp.

Overall, plagioclase grain sizes increase with decreasing temperature (Table 3). Plagioclase growth rates were calculated assuming a constant cooling rate of 1 °C/h from the time when the experimental charge reached 1050 °C (when plagioclase starts nucleating) to when it was quenched (Fig. 1), and using the maximum observed long axis of the plagioclase grains as viewed in the 2D images. This results in calculated plagioclase growth rates of 1.39×10^{-10}–2.32×10^{-10} m/s (Table 3).

Regardless of the temperature on quenching, plagioclase aspect ratios in our experimental charges are constant at ~2.1 (Table 3), with the exception of those in the charges that were not prepared in the muffle furnace (Table 2). These charges have a higher plagioclase aspect ratio of 4.3 and a faster plagioclase growth rate of 1.05×10^{-9}–1.52×10^{-9} m/s (Table 3). There is no relationship between the prevalence and size of Fe-rich droplets, and either plagioclase aspect ratio, grain size or growth rate.
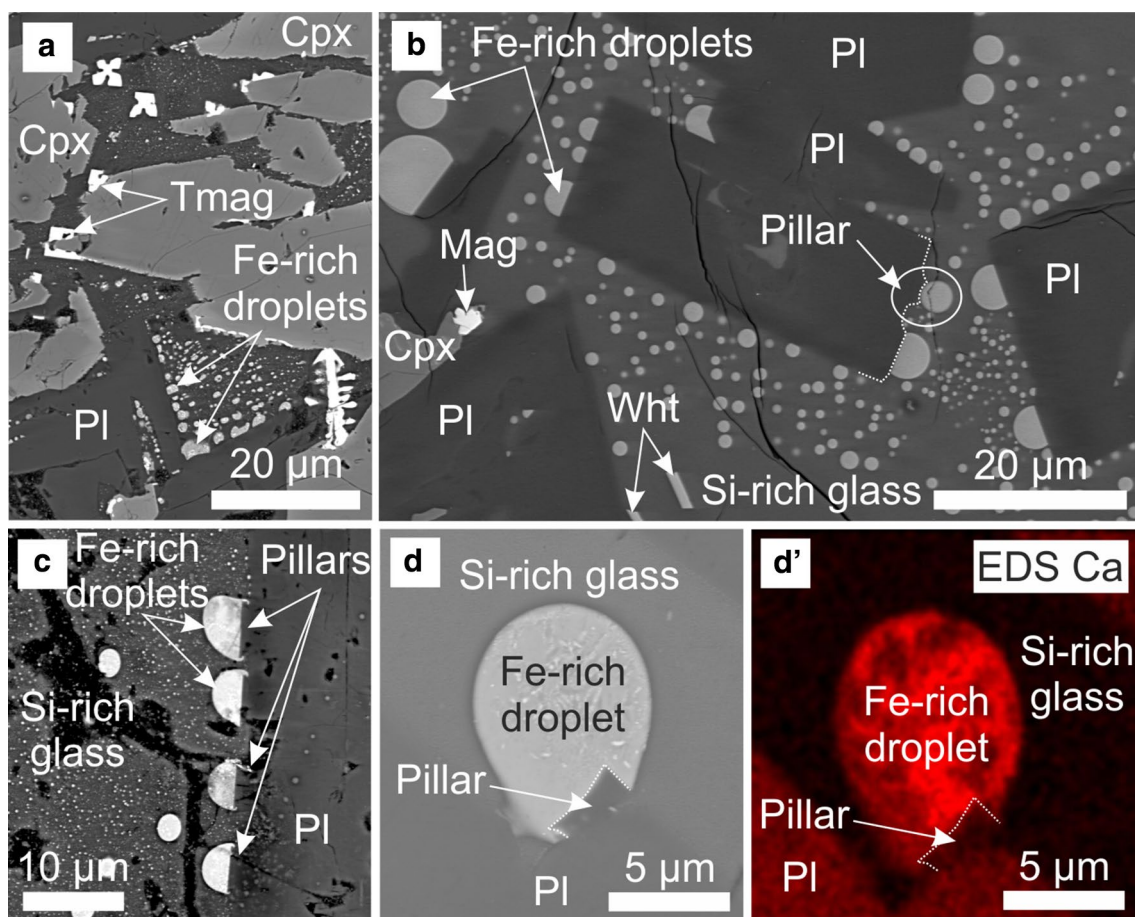
Magnetite

Below 1025 °C, magnetite locally develops feathery fringes, analogous to the pyroxene marginal growth structures, on at least two, but not all, of the intersected crystal faces (Fig. 2a). The elongated oval-shaped grains in the fringe are whitlockite. Feathery fringes are also visible on magnetite in natural samples from the Cohasset lava flow, USA. Fe-rich droplets wet the surface of magnetite with a low wetting angle against the sharply defined planar growth face of the magnetite (Table 4). Fe-rich droplets do not wet a surface with a feathery fringe. At lower temperatures (< 1005 °C), Fe-rich droplets commonly wet magnetite grains, which tend to form clusters and are commonly associated with tabular grains of whitlockite.

Glass compositions

Constant cooling experiments

In experimental charges quenched above 1030 °C (i.e., above the binodal), the glass phase has relatively constant major element concentrations (S. Table B). Minor incompatible elements such as ZrO_2, Y_2O_3 and P_2O_5, increase in concentration in the glass as crystallisation progresses. For example, P_2O_5 concentrations in the glass rose from 0.8 wt% at 1150 °C to 1.2 wt% at 1050 °C. With the onset of unmixing apparent at 1030 °C, the Si-rich glass SiO_2 concentration increases down temperature from 57 to 70 wt% at 955 °C: the opposite trend is observed for FeO, which decreases in concentration in the Si-rich glass at lower temperatures. Similarly, ZrO_2, Y_2O_3 and P_2O_5 decrease in the Si-rich glass (Ce_2O_3 was below EPMA detection). The P_2O_5 concentration decreases from 1.3 wt% at 1030 °C, to 0.5 wt% at 955 °C. Note that crystallisation and unmixing occur simultaneously: the onset of

Fig. 4 Microstructures in BSE images from **a** the Cohasset flow, USA, showing epitaxial growth of titanomagnetite along planar pyroxene faces and feathery fringes on pyroxene, **b** from the experiments: plagioclase laths with pillar structures along crystal faces, enclosed by an attached Fe-rich droplet of slightly larger diameter than the pillar, **c** from the Cohasset flow: pillar structures, enclosed by Fe-rich droplets on plagioclase, **d** from the Kilauea Iki lava lake: a pillar structure enclosed by an Fe-rich droplet on plagioclase, **d'** a Ca EDS map of image (**d**)

Table 3 Plagioclase apparent sizes and growth rates

Run	Final temp (°C)	No. plag	Min size (µm)	Max size (µm)	Av size (µm)	Aspect ratio (AR)	Growth rate (max) m/s	Growth rate (av) m/s	Plag modal %
VIC08	1050	285	3.19	60.92	13.83	1.80	2.29E−10	5.19E−11	16
VIC06	*1030*	*273*	*9.65*	*513.09*	*78.97*	*4.68*	*1.52E−09*	*2.33E−10*	*27*
VIC08	1025	397	3.95	82.66	19.60	2.34	2.32E−10	5.50E−11	32
VIC08	1010	295	3.92	57.00	20.10	2.18	1.39E−10	4.90E−11	29
VIC06	*1010*	*267*	*7.59*	*431.84*	*83.11*	*3.96*	*1.05E−09*	*2.03E−10*	*27*
VIC07	1005	333	3.24	72.20	17.62	2.38	1.69E−10	4.11E−11	31
VIC09	1000	269	6.35	90.01	26.08	2.11	2.02E−10	5.84E−11	35
VIC09	980	371	5.81	76.99	22.80	2.12	1.49E−10	4.40E−11	36
VIC09	955	460	4.04	100.18	22.19	2.34	1.65E−10	3.65E−11	43

Italicised final temperature values denote experiments prepared @ QFM

Table 4 Wetting angle (WA) measurements of the Fe-rich droplets attached to mineral phases for the experiments presented here and measurements collected from experiments with a Mull and Sept Iles starting composition from the study of Charlier and Grove (2012)

Run	Final temp (°C)	Dwell time (h)	Plag median WA (°)	No. of WA	− ve 2σ	+ ve 2σ	Oxide median WA (°)	No. of WA	− ve 2σ	+ ve 2σ
Experiments from this study										
VIC06	*1030*	*0*	*81*	*29*	*12*	*8*	–	–	–	–
VIC08	1025	0	93	196	2	2	–	–	–	–
VIC08	1010	0	101	112	3	3	24	21	11	2
VIC06	*1010*	*0*	*121*	*143*	*2*	*2*	*25*	*6*	*5*	*14*
VIC07	1005	0	115	122	4	5	–	–	–	–
VIC09	1000	0	118	210	3	3	23	38	4	3
VIC09	980	0	125	121	3	3	26	40	2	2
VIC09	955	0	127	221	3	2	33	29	5	7
VIC10	1021	12	112	119	5	4	–	–	–	–
VIC10	1021	40	108	189	2	5	–	–	–	–
VIC10	1021	158	114	85	1	2	–	–	–	–
VIC06	*1000*	*18*	*118*	*168*	*1*	*2*	*23*	*14*	*7*	*3*
VIC07	1000	62	121	141	2	2	20	44	2	3
VIC07	1000	182	119	101	3	4	20	30	8	8
Sept Iles experiments (experimental details in Charlier and Grove 2012)										
SI-5	1006	96	118	54	2	6	–	–	–	–
SI-8	963	48	120	83	2	3	–	–	–	–
SI-9	938	72	123	105	1	2	–	–	–	–
Mull experiments (experimental details in Charlier and Grove 2012)										
M-9	1020	64	74	122	3	3	–	–	–	–
M-5	1005	92	81	103	3	2	–	–	–	–
M-6	963	48	86	108	1	2	–	–	–	–
M-7	938	72	91	56	3	3	–	–	–	–

Italicised final temperature values denote experiments prepared @ QFM

unmixing coincides with the onset of whitlockite crystallisation, and the observed decrease in P_2O_5 concentration in the Si-rich glass is thus a consequence of both whitlockite crystallisation and the unmixing of a Fe-rich liquid.

The FeO concentration of those Fe-rich droplets large enough to be analysed by EPMA increases steadily from 22 to 24 wt%, as the temperature decreases from 1025 to 955 °C. Likewise, ZrO_2, Ce_2O_3 and P_2O_5 increase in the (larger) Fe-rich droplets: P_2O_5 rises from 5.7 wt% at 1025 °C to 11.7 wt% at 955 °C. Over the same temperature interval, SiO_2 concentration in the Fe-rich droplets decreases from 38 to 29 wt%.

We plot our glass composition data as a function of NBO/T (where NBO is the number of non-bridging oxygens, T is the tetrahedrally coordinated network forming cations: Si + Al + P + Ti). This can be used as a measure of the degree of polymerisation in silicate melts (Mysen 1983). The NBO/T for Fe-rich droplets increases with decreasing temperature; conversely, the NBO/T for the Si-rich phase decreases. Thus, the immiscibility field expands with

decreasing temperature (Fig. 5). The density of the Si-rich glass [calculated according to Bottinga and Weill (1970)] decreases from 2.6 to 2.4 g/cm^3 over an experimental temperature drop of 1025–955 °C. The density of Fe-rich glass increases from 2.9 to 3.0 g/cm^3 over the same 70 °C interval (S. Table B). The calculated viscosity (Giordano et al. 2008) for liquids with the composition of the Si-rich glass increases from 10^4 Pa.s at 1050 °C to 10^7 Pa.s at 955 °C. The calculated viscosity for the corresponding Fe-rich liquid remains relatively constant as temperature decreases, with a viscosity ranging from 10^4 to 10^3 Pa.s (S. Table B).

Isothermal experiments

The SiO_2 concentration in the Si-rich glass increases from 66 to 69 wt% over the 146 h that the experimental charges were held at 1021 °C; and from 66 to 71 wt% over the 164 h the charges were held at 1000 °C. FeO concentrations in the Si-rich glass decrease with longer isothermal dwell times, from 7.0 to 4.7 wt% FeO between experimental charges t_{12} and t_{158} at 1021 °C, and from 7.5 to 4.1 wt% FeO between
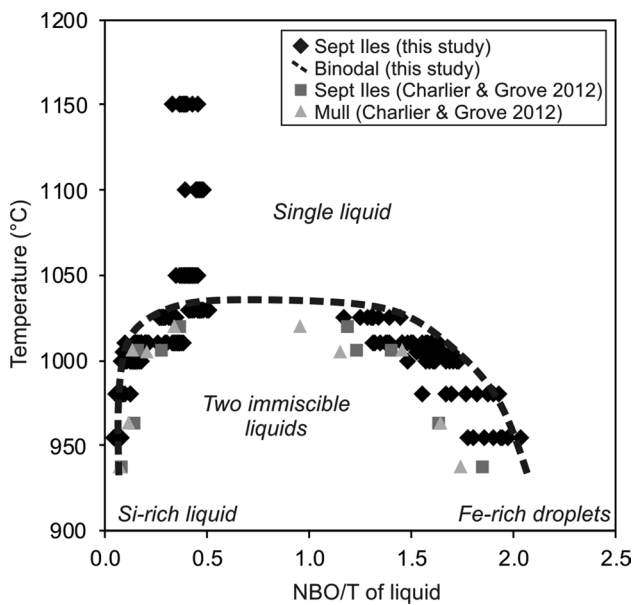
Fig. 5 Temperature as a function of the degree of polymerisation (NBO/T, $T = Si + Al + P + Ti$), the dashed line represents the maximum compositional space where these experiments show evidence of unmixing. As a comparison, immiscible liquid analyses are plotted from Charlier and Grove (2012) for Sept Iles and Mull compositions

experimental charges t_{18} and t_{182} at 1000 °C. Consequently, the NBO/T values for the Si-rich glass decrease as dwell time increases.

Conversely, the NBO/T and Mg# of the Fe-rich droplets increase with isothermal dwell time, as does the concentration of P_2O_5, Ce_2O_3 and ZrO_2. The concentration of P_2O_5 increases by 50% over 146 h (from 8.9 to 13.3 wt%) in experimental charges held at 1021 °C prior to quenching, and 148% over 164 h (from 5.9 to 14.6 wt%) in experimental charges held at 1000 °C. The SiO_2 concentration of the Fe-rich droplets decreases with dwell time; there is a faster rate of decrease in the experimental charges held at the 1000 °C isothermal plateau compared to those held at 1021 °C.

Wetting angles

The population of measured apparent wetting angles of the Fe-rich liquid on plagioclase is typically unimodal (S. Figure A), with the exception of that in the experiment quenched at 1030 °C which is bimodal. The 3D wetting angle (determined as the median of the population of 2D apparent wetting angles) increases as the temperature decreases from 93° ± 2° at 1025 °C to 127° ± 3° at 955 °C (Table 4, Fig. 6a). The largest wetting angle is associated with the lowest NBO/T value of the surrounding Si-rich phase and the highest NBO/T value of the Fe-rich phase, i.e., when the continuous phase is most polymerised and the Fe-rich phase is least polymerised (Fig. 6b). The wetting angles do

not vary as a function of increasing isothermal dwell time prior to quenching (Fig. 6c).

The wetting angle of Fe-rich droplets on oxides is constant at ~ 24° between 1030 and 1005 °C, increasing to 33° ± 6° at 955 °C. While the number of wetting angle measurements of Fe-rich droplets on pyroxene were insufficient to provide a statistically robust median value, the measurements obtained suggest angles between 23° and 32° over the temperature range 1025–980 °C. Additional wetting angle measurements were made on the Charlier and Grove (2012) experimental charges with a Mull and Sept Iles starting composition (Table 4); these corroborate the trends from our experiments.

Nucleation kinetics
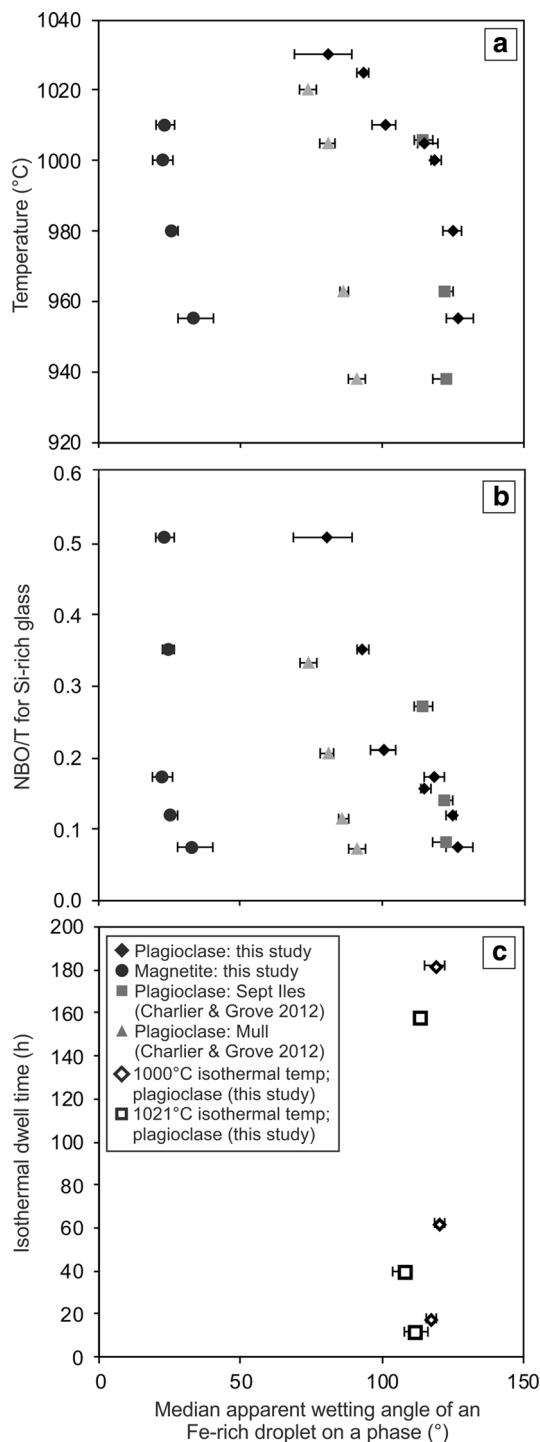
Volume of immiscible liquid

In experimental charges that were continuously cooled (1 °C/h) and then quenched, the proportion of Fe-rich droplets in the glass increases and then decreases relative to the continuous Si-rich phase with decreasing temperature. At 1025 °C, the Fe-rich droplets comprise 5 vol.% of the total glass; at 1000 °C they comprise 7 vol.%; and at 955 °C they comprise 4 vol.% (Table 5). This trend follows that of the relative percentages of the two phases calculated from the asymmetric silicate liquid immiscibility binodal (Fig. 5). In experimental charges with longer isothermal dwell times, the proportion of Fe-rich glass decreases.

Droplet size distribution: constant cooling evolution

A preliminary evaluation of the size and number of Fe-rich droplets as a function of temperature after cooling at a constant rate can be made by inspecting Fig. 2. The number density of Fe-rich droplets (as viewed in 2D, combining both attached and isolated droplets) decreases between 1025 and 955 °C, from 72 to 33 Fe-rich droplets per mm² of glass (Table 5). There is little variation in the number of attached droplets over the investigated temperature interval, whereas the number of isolated droplets decreases.

During constant cooling from the onset of unmixing to 1000 °C, attached droplets have a larger average effective diameter as viewed in 2D (d_{AT}), and 2D area than isolated droplets (d_{IS}) (Figs. 7 and 8). The d_{IS} increases with decreasing temperature, from 0.78 to 0.98 μm. Below 1000 °C, isolated and attached droplets have comparable average effective diameters (Table 5).

The droplet size distributions (DSD) for attached Fe-rich droplets at different temperatures have a constant maximum number density and a constant droplet diameter at that maximum number density (d_{AT}*; Fig. 8a). The range of d_{AT} is < 1 to 22 μm. With decreasing temperature, the

Fig. 6 Wetting angle for the Fe-rich immiscible liquid plotted against **a** temperature; **b** NBO/T for the Si-rich liquid, where $T = Si + Al + P + Ti$, which represents the degree of polymerisation of the surrounding liquid; **c** wetting angle for the Fe-rich droplets on plagioclase plotted against dwell time (h)

gradient of the DSDs for attached droplets remains constant. For isolated droplets, the maximum number density decreases with decreasing temperature, simultaneously with

an increase in the droplet diameter at that maximum number density ($d_{AT}*$). The d_{AT} and d_{IS} is within bin size error of $d_{AT}*$ and $d_{IS}*$. Between 1025 and 1005 °C, the d_{IS} range is 0.5–3 μm. At lower temperatures, this doubles to 6.5 μm (Fig. 8b). The DSDs for isolated droplets have a steeper gradient to larger droplet sizes (for each experimental charge) than the DSDs for attached droplets. Nevertheless, as temperature decreases, the gradient of the isolated droplet DSDs decreases.

Droplet size distribution: isothermal evolution

The number density of all Fe-rich droplets (normalised to modal glass) decreases as the dwell time at constant temperature increases (Table 5). In detail, the number density of isolated Fe-rich droplets decreases with a significantly steeper gradient than attached Fe-rich droplets.

At shorter dwell times, the DSDs for Fe-rich droplets have a wider range of droplet diameters (Fig. 9): 0.25– > 10 μm for d_{AT} and 0.25–6 μm for d_{IS}. These ranges halve for experimental charges with isothermal dwell times longer than 150 h. The attached droplets have a constant maximum number density and the droplet diameter at the maximum number density ($d_{AT}*$) is relatively consistent (Fig. 9). The exception is a decrease in maximum number density of attached Fe-rich droplets in the experimental charge t_{158}, which was quenched at 1021 °C. The DSDs have a positive slope for $d_{IS} < d_{IS}*$, where $d_{IS}*$ is the isolated droplet diameter at the maximum number density. For the isolated Fe-rich droplets, the maximum number density decreases in the experimental charges held for an increasing dwell time at both temperatures. The $d_{IS}*$ is constant for experimental charges t_{12}–t_{158} held at 1021 °C, while for t_{18}–t_{182}, held at 1000 °C, the $d_{IS}*$ doubles from 0.4 μm at t_{18} to 0.8 μm at t_{182}. The gradient of the isolated DSDs is steeper than that of the attached DSDs for all experimental charges regardless of isothermal dwell time or quench temperature.

The location of nucleation of immiscible droplets

Isolated Fe-rich droplets are volumetrically more significant than attached Fe-rich droplets in the experimental charges with no isothermal dwell time. The number of potential sites for heterogeneous nucleation of Fe-rich droplets on plagioclase grains is a function of the area of plagioclase surfaces but as modal plagioclase increases from 27% at 1030 °C to 43% at 955 °C, the ratio of the total area of isolated/attached Fe-rich droplet also increases, while the ratio of the numbers of isolated/attached Fe-rich droplets decreases. There is a positive correlation between the ratio of isolated/attached Fe-rich droplet areas and the wetting angle of Fe-rich droplets on plagioclase for angles > 90° (Fig. 10a). When the wetting angle is < 90°, there is a negative correlation between

Table 5 Fe-rich droplet size distributions

Final temp (°C)	Dwell time (h)	Modal glass %	Droplets/mm² of glass	Mean d_{IS} (µm)	Mean d_{AT} (µm)	Max d_{IS} (µm)	Max d_{AT} (µm)	Density change (kg/m³)	$D_{4,3}/D_{3,2}$
1030	0	66	2	0.48	0.49	0.92	0.64	–	–
1025	0	54	72	0.78	1.01	3.55	4.23	420	1.13
1010	0	57	37	0.76	0.91	2.24	3.80	510	1.09
1010	0	59	70	0.54	1.18	4.03	22.26	400	1.46
1005	0	55	23	0.91	0.96	3.79	3.51	560	1.17
1000	0	53	75	0.85	1.18	6.47	9.06	530	1.21
980	0	47	47	0.96	0.91	5.76	5.75	590	1.19
955	0	43	33	0.98	1.00	4.51	4.62	640	1.21
1021	12	63	20	0.85	0.89	3.26	4.73	470	1.14
1021	40	61	39	0.72	1.07	3.3	5.91	490	1.17
1021	158	53	6	0.69	1.01	1.84	3.26	510	1.11
1000	18	60	80	0.63	0.97	5.87	9.38	480	1.50
1000	62	54	38	0.85	1.00	7.76	5.42	590	1.54
1000	182	50	21	0.81	0.95	3.22	3.45	580	1.09

d_{IS} = isolated Fe-rich droplet diameter, d_{AT} = attached Fe-rich droplet diameter. ($D_{4,3}/D_{3,2}$) is the ratio of the Fe-rich droplet volume-weighted mean diameter versus the surface-weighted mean diameter, following Farr et al. (2017)
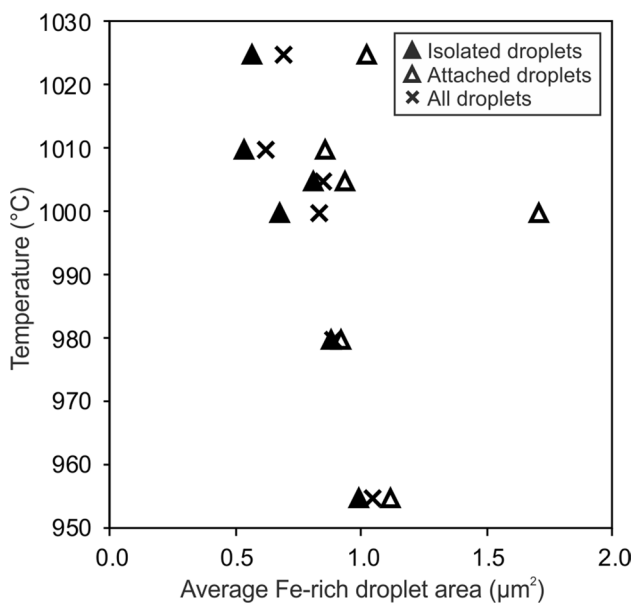
Fig. 7 The average area of Fe-rich droplets (µm²) plotted against temperature for experiments that underwent constant cooling at 1 °C/h

the wetting angle on plagioclase and the ratio of isolated/attached Fe-rich droplet areas, as shown by the experiments with a Mull composition. The ratio of isolated/attached Fe-rich droplet numbers decrease with decreasing quenching temperature for the Mull composition experiments.

The ratio of isolated/attached Fe-rich droplets in terms of both area and number decreases in experimental charges held for longer isothermal dwell times prior to quenching (i.e. more droplets are attached at longer dwell times;

Fig. 10b). The gradient decrease is steeper for experimental charges held isothermally at 1021 °C compared to 1000 °C.

Influence of the super-liquidus history on droplet nucleation and growth

The effect of the initial thermal history above the liquidus was explored with two experiments quenched at 1010 °C: one being part of the experimental run VIC08 [herein referred to as 1010(8)] and the other being part of the experimental run VIC06 [herein referred to as 1010(6)] (Table 2). Both experimental charges underwent a constant cooling rate of 1 °C/h, with no dwell time before quenching, but the immiscibility microstructures differ. The preparation of the two charges was different prior to commencement of the constant cooling rate experiments (Table 2): experimental run 1010(8) was heated to 1150 °C in a muffle furnace in air, whereas experimental run 1010(6) was heated to 1104 °C at QFM. Experiment 1010(6) contains an order of magnitude more Fe-rich droplets than experiment 1010(8), with the majority of droplets smaller than 1 µm² (as viewed in 2D). In experiment 1010(8) the majority of droplets are smaller than 2 µm² (Table 5). The plagioclase aspect ratio in experiment 1010(6) is 4.0, (the crystals are dendritic) while in experiment 1010(8) the aspect ratio is 2.2, consistent with the other experimental charges that were prepared in the muffle furnace (Table 3). Hence, experimental preparation has an influence on nucleation and growth rates (see "Homogeneity of the starting liquid" in the "Discussion" section).
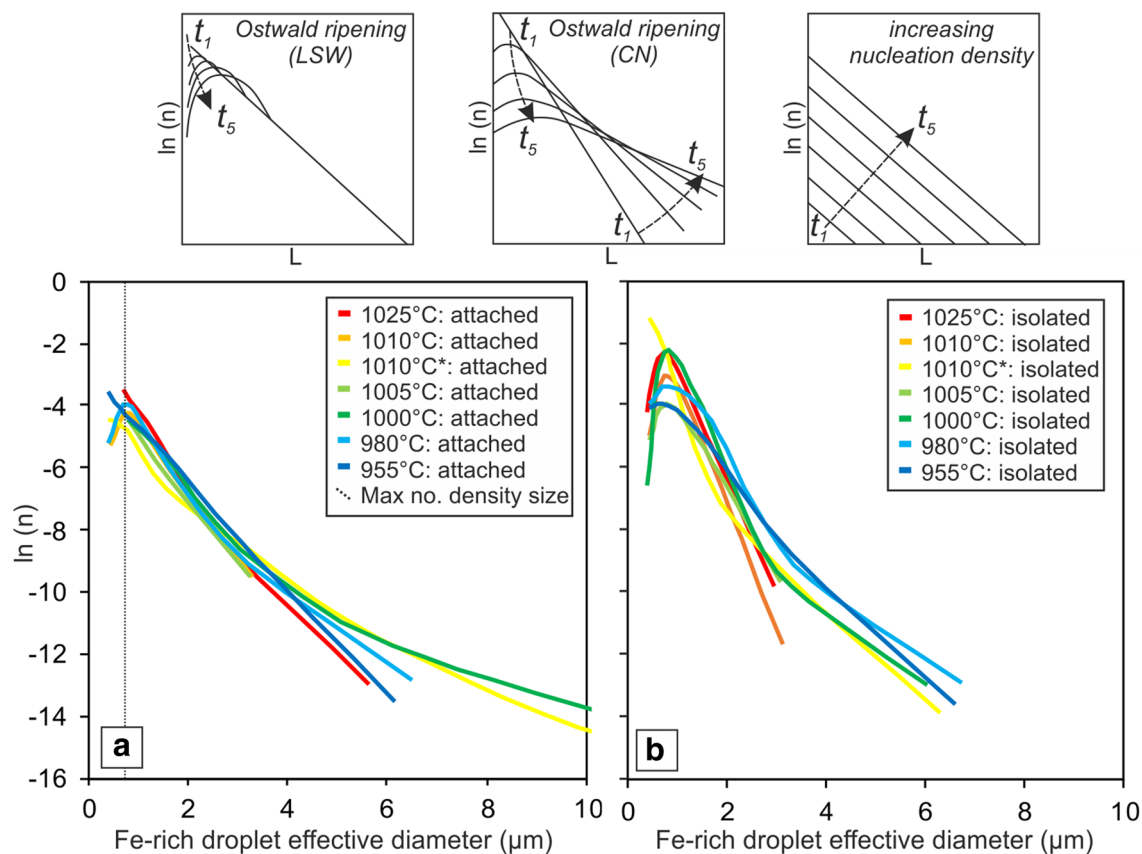
Fig. 8 Droplet size distribution (DSDs) for experiments that have undergone constant cooling at 1 °C/h. **a** DSDs for Fe-rich droplets attached to plagioclase. **b** DSDs for Fe-rich droplets not in contact with a crystal phase in the 2D view (isolated). 1010 °C. * indicates that this experimental charge underwent different preparation to the other experiments (see Table 2). The grey insets are theoretical dispersions of crystal size distributions after Higgins (2002); and Marsh (1988): LSW theory (Lifshitz and Slyozov 1961; Wagner 1961) assumes a particle's coarsening rate is independent of its surroundings; the "communicating neighbours" (CN) theory (DeHoff 1991) assumes only particles in close proximity affect the other's evolution

Discussion

Nucleation processes: homogeneous or heterogeneous?

Onset of unmixing

At the onset of silicate liquid unmixing, isolated Fe-rich droplets dominate. The narrow size distribution of the Fe-rich droplets, and their (apparent) isolation in the continuous Si-rich liquid, are consistent with a short interval of (homogeneous) nucleation. Homogeneous nucleation is likely to be promoted by the small compositional difference between the immiscible liquids which leads to a low energy interface between the two liquids (Veksler et al. 2010).

Droplet nucleation as the binodal widens

At lower temperatures, the compositional difference between the two immiscible liquids increases (Fig. 5), increasing the energy of the interface separating the two phases (Veksler et al. 2010). As temperature decreases, isolated droplets remain abundant suggesting that homogeneous nucleation remains important; however, the number of isolated droplets decreases with decreasing temperature, simultaneously with increasing average droplet size.

At temperatures 10–20 °C below the onset of unmixing, the undercooling is relatively small. In isothermal experiments held at 1010 °C (after constant cooling at 1 °C/h), the number of isolated Fe-rich droplets decreases (likely due to coarsening—see later), but there is no increase in the nucleation density (as shown by the DSDs, Fig. 9), even after an isothermal dwell time greater than 150 h.

Small degrees of undercooling make it energetically favourable to nucleate droplets heterogeneously on crystal faces. Plagioclase is the dominant phase for heterogeneous nucleation of the Fe-rich liquid (Fig. 11). This is perhaps surprising because Fe-rich liquids are more likely to wet a mafic phase (e.g. Holness 2006; Jakobsen et al. 2005; Philpotts 1977; Vukmanovic et al. 2018) as also shown by our
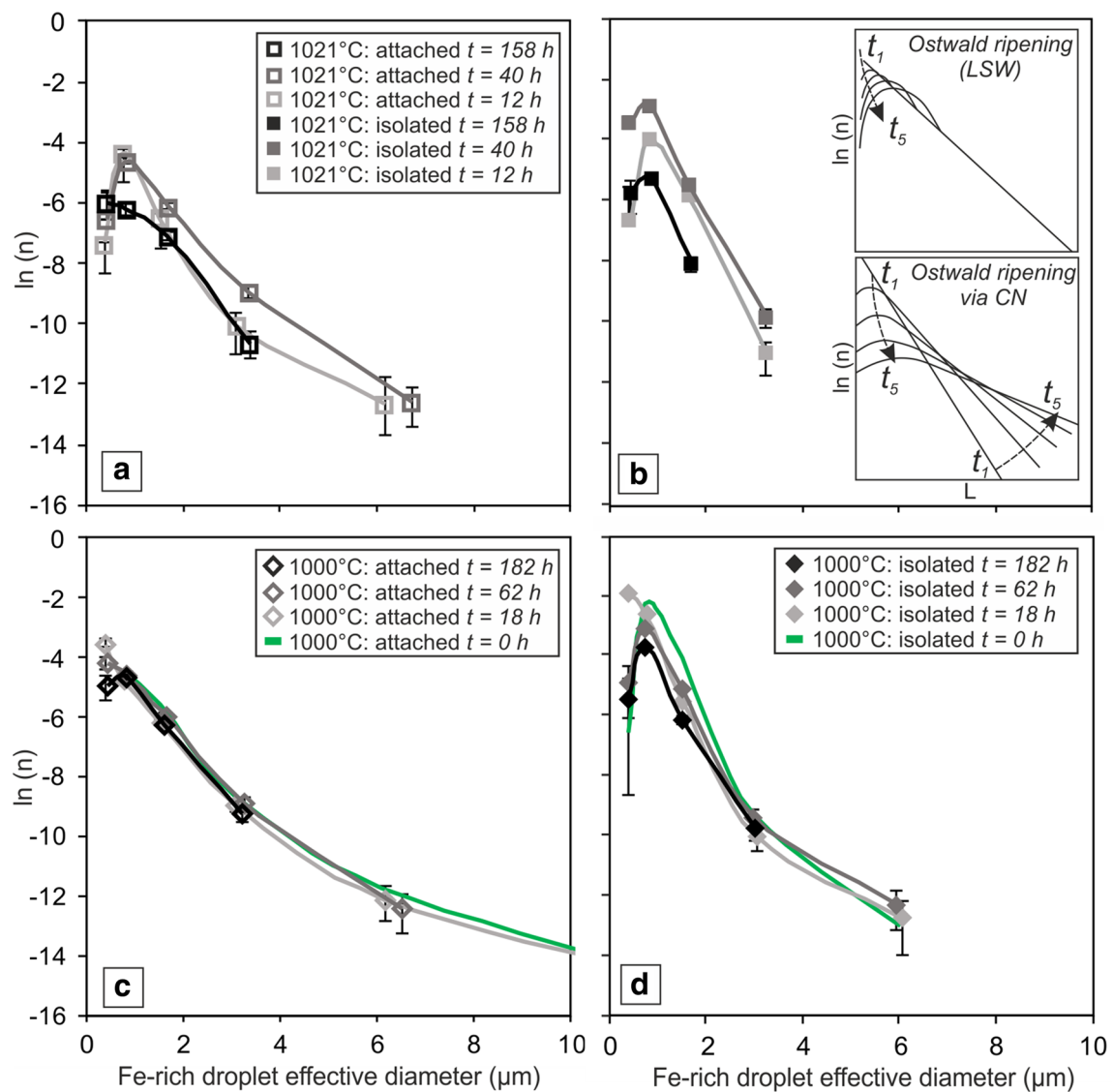
Fig. 9 Droplet size distribution (DSDs) for experimental charges that have been held isothermally. **a** DSDs for Fe-rich droplets attached to plagioclase held at 1021 °C between t_{12} to t_{158}. **b** DSDs for isolated Fe-rich droplets in the 2D view, held at 1021 °C between t_{12} and t_{158}. **c** DSDs for Fe-rich droplets attached to plagioclase held at 1000 °C between t_{18} and t_{182}. **d** DSDs for isolated Fe-rich droplets in the 2D view, held at 1000 °C between t_{18} and t_{182}. For comparison in (**c**, **d**), the attached and isolated DSDs for the experiment quenched at 1000 °C with no isothermal dwell time are plotted. The insets are theoretical dispersions of crystal size distributions after Higgins (2002); and Marsh (1988)

wetting angle measurements. Kinetic processes must therefore play a role. We suggest the Fe-rich liquid distribution in the quenched experiments is controlled by the creation of compositional boundary layers (CBL) around the growing grains (Zellmer et al. 2016): compositional boundary layers adjacent to plagioclase will be enriched in Fe, Ti, Mg, and P, promoting unmixing and heterogeneous nucleation of Fe-rich droplets. Conversely, any compositional boundary layer developing around growing grains of whitlockite will be depleted in P, thus decreasing the size of the silicate

liquid immiscibility field in composition space (Bogaerts and Schmidt 2006; Charlier and Grove 2012; Visser and Van Groos 1979), and inhibiting unmixing in the adjacent liquid. While there is no obvious control by temperature, with the density of heterogeneously nucleated Fe-rich droplets on plagioclase crystal faces being constant in experiments with continuous cooling (as shown by DSDs, Fig. 8), a further factor might be the nature of the underlying structure of the crystal surface, with the plagioclase surface providing a particularly favourable substrate (e.g. Pleše et al. 2018).
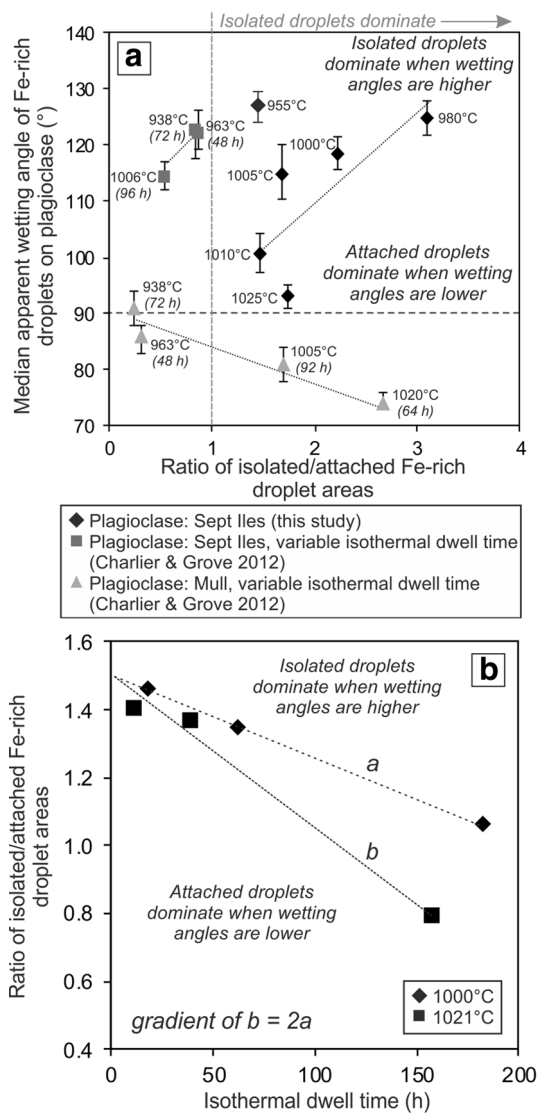
Fig. 10 a The ratio of isolated/attached Fe-rich droplet areas plotted against the wetting angle of Fe-rich droplets on plagioclase for these experiments, and Charlier and Grove (2012) experiments using a Sept Iles and Mull composition. **b** The ratio of isolated/attached Fe-rich droplet areas plotted against dwell time (h)

Note, however, that we do not observe a continuous Fe-rich film surrounding plagioclase grains, as seen in natural samples and some experiments (Morse and Brady 2017; Hartley pers comm 2019). We suggest the absence of the continuous film of unmixed Fe-rich liquid and the presence, instead, of discrete droplets could be controlled by the growth rate of the plagioclase. The maintenance of continuous films of Fe-rich liquid, which our wetting angle measurements demonstrate are in textural disequilibrium, requires plagioclase growth rates to be significantly faster than that of chemical diffusion in the surrounding liquid. The average plagioclase aspect ratio is 6.0 in the natural samples in which continuous Fe-rich films are observed (e.g.,

the Kilauea Iki lava lake) but only 2.1 in our experiments. Lower plagioclase aspect ratios imply slower growth (Holness 2014; Sato 1995), so we suggest that the plagioclase aspect ratios in our experiments are consistent with growth rates that were too low to maintain texturally disequilibrium Fe-rich compositional boundary layers.

The CBLs developing around magnetite and pyroxene are enriched in elements such as Si, Al, and Na, consistent with the absence of droplets in the vicinity of these phases (Si-rich CBLs). This is reversed at lower temperatures and, as temperatures decrease, Fe-rich droplets increasingly wet the surface of magnetite and pyroxene. The low wetting angles (23°–33° for oxides and 23°–32° for pyroxenes; Table 4) show that this spatial relationship is more energetically favourable than that of an Fe-rich liquid wetting plagioclase (Holness 2006): thus this trend towards a concentration of Fe-rich liquid adjacent to mafic phases represents a transition towards textural equilibrium rather than a change in the nucleation kinetics.

Homogeneity of the starting liquid

Spatial compositional variations in the starting liquid have a significant effect on the abundance of droplet nucleation sites; Lofgren (1983) showed that experimentally heating a basaltic magma for 1 h, 10 °C above the plagioclase saturation limit, removed all plagioclase nuclei and hence inhibited plagioclase crystallisation. Consequently, the experimental charge preparation conditions will affect the number of available nucleation sites both for the exsolving Fe-rich liquid and for crystalline phases. Experiment 1010(6) resulted in anomalously large dendritic crystals with large numbers of very small Fe-rich droplets (< 1 μm^2), whereas experiment 1010(8) resulted in a crystal microstructure typical of the experiments comprising smaller, subhedral crystals and a lower number of Fe-rich droplets. Dendritic crystals grow under conditions of diffusion-limited growth, which is commonly caused by a large undercooling (e.g. Mullis 2003). We suggest that a low nucleation rate in experiment 1010(6) permitted a large undercooling to develop, resulting in the growth of a few, large (dendritic) crystals. The large, scattered dendritic crystals resulted in the creation of relatively large interstices between crystals, promoting homogeneous droplet nucleation (Holness and Sawyer 2008; Putnis and Mauthe 2001).

We attribute these microstructural differences to the experimental charge preparation. Experiment 1010(6) was heated to 1104 °C and held for 16 h, while experiment 1010(8) was heated to 1150 °C and held for only several minutes: we suggest the longer duration of the isothermal hold led to a greater reduction of crystal nucleation sites in 1010(6). Another potential difference is the Fe content of the Fe-electroplated platinum loop on which the charge was
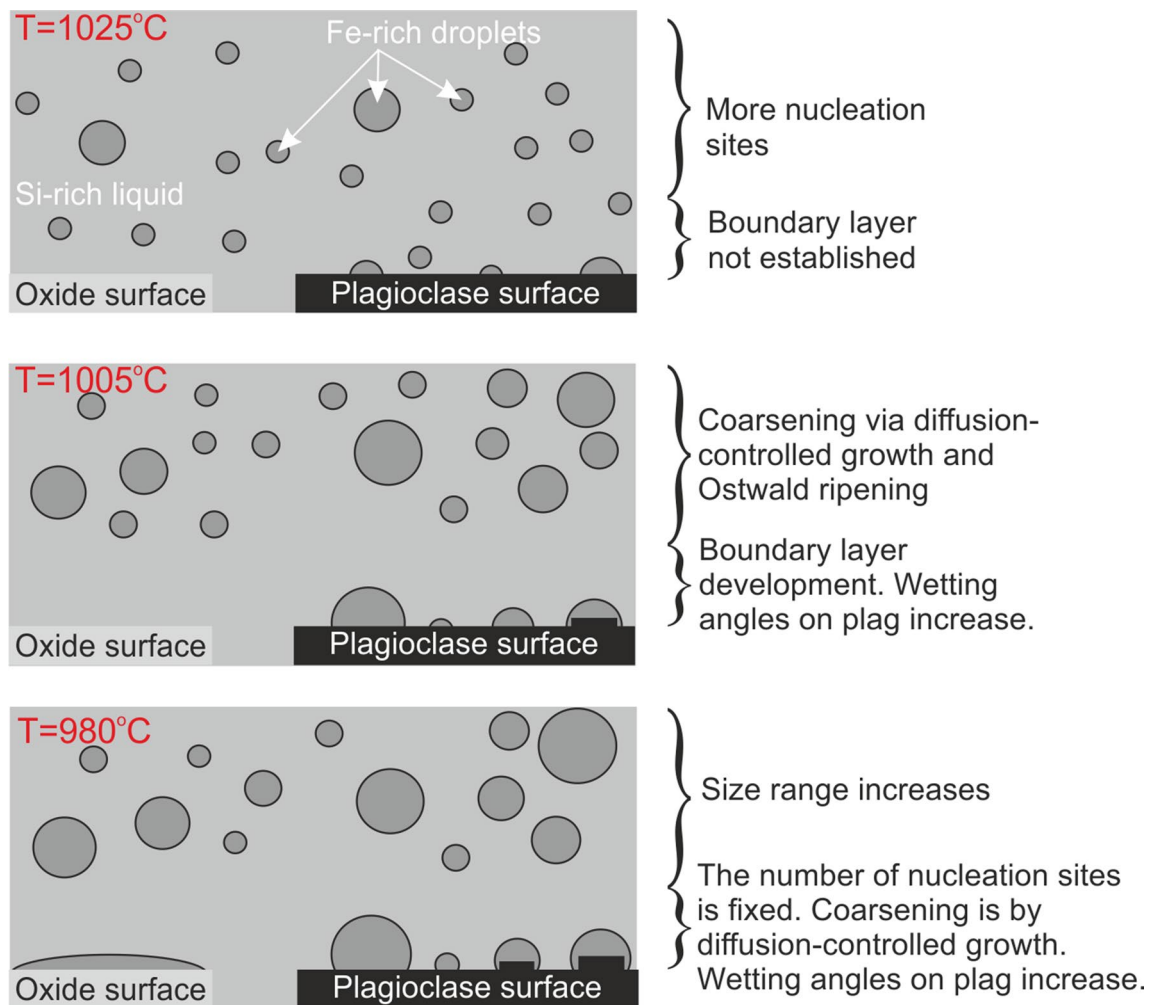
Fig. 11 Schematic illustration of the evolution of the physical behaviour of the unmixing liquids as temperature decreases

suspended: this could have affected the FeO content of the charge. If experiment 1010(6) had a slightly higher bulk Fe content, combined with the lower energy required to nucleate liquid droplets, this could produce the microstructural differences observed.

Microstructural indicators of immiscibility in solidified mafic rocks

Our experimental charges show that microstructural features of the mineral grains develop in conjunction with unmixing of their host liquid. Such features, if recognised in natural examples of fully solidified rocks in which there is no preserved record of liquid unmixing, could potentially be used as a marker for the occurrence of liquid immiscibility during solidification.

Pyroxene and magnetite feathery fringes

In experimental charges quenched at 1050 °C, most grains are equant with smooth planar crystal faces, demonstrating that crystal growth was mainly interface controlled. Experimental charges quenched below 1030 °C (i.e. the onset of unmixing for the liquid compositions used for our experiments) contain Fe-rich droplets that wet the surface of magnetite and pyroxene grains. These Fe-rich droplets are only present on euhedral grain surfaces, indicative of interface-controlled growth. In contrast, the feathery fringes on pyroxene and magnetite, associated with whitlockite, are consistent with diffusion-limited growth and therefore the creation of a CBL surrounding pyroxene and magnetite. Such feathery fringes have the potential to be used as microstructural indicators of unmixing during solidification.

Phosphorus is incompatible in pyroxene, with a clinopyroxene–basaltic liquid partition coefficient ranging between 0.01 and 0.05 (Anderson and Greenland 1969; Brunet

and Chazot 2001). If the pyroxene growth rate (typically 1×10^{-7} m/s (Dunbar et al. 1995; Kouchi et al. 1983)) exceeds the P chemical diffusion rate in the silicate liquid [~ 3.5×10^{-11} m^2/s, for a basaltic liquid; Chen and Zhang (2008), (2009); Lundstrom et al. (2005)] then P would be enriched in a boundary layer surrounding a growing pyroxene. As crystallisation proceeds, incompatible elements are enriched in the silicate liquid surrounding the growing pyroxene and magnetite. This forms a CBL within which whitlockite nucleates, and where the rate of material transport is likely set by the least mobile component which, in the case of whitlockite, is P. The microstructures we describe suggest that small grains of whitlockite that nucleate and grow in the CBL are either engulfed by the growth of their pyroxene substrate, or that the larger whitlockite grains stunt further pyroxene growth. We suggest that the variation in width of the pyroxene feathery fringes on different growth faces in our experiments is due to variations in pyroxene growth rates (Kouchi et al. 1983).We could not quantify a consistent preferred crystallographic relationship between whitlockite and augite by EBSD, and suggest that further EBSD work is required to definitively establish the crystallographic relationship between these two phases. P and Ca are incompatible in magnetite, and so the same mechanism outlined for pyroxene could destabilize planar growth faces of magnetite by the development of CBLs.

A remaining question is why P- and Ca-rich phases form as a result of CBL development around pyroxene, when pyroxene growth should also cause enrichment in elements such as Al and Na in the CBL. This could, perhaps, be due to the much faster chemical diffusion rates of Al and Na in a silicate liquid that preclude the development of CBLs defined by spatial variations of these elements.

Plagioclase pillars

The observed pairing of albitic pillars and Fe-rich droplets (Fig. 4d') could result from either the heterogeneous nucleation of the droplet on the surface of a pre-existing pillar, or formation of the pillar by growth from a Fe-rich liquid after heterogeneous nucleation of the droplet on an originally planar plagioclase crystal face. If the former, then we might expect pillars to be a commonly observed feature of rapidly cooled basalts in which diffusion-limited growth occurs, but they are not (Helz and Wright 1992; Neave et al. 2017). Consequently, following Philpotts (1981), we suggest that pillar formation post-dates the attachment of the Fe-rich droplets, and that the presence of a Fe-rich droplet destabilizes the plagioclase planar growth face, resulting in localised enhanced growth of plagioclase.

This hypothesis is supported by the enrichment of the pillars in elements with a low concentration in the Fe-rich immiscible liquid, such as Na, Al and Si (Veksler et al.

2006). Since the two conjugate liquids become more compositionally distinct with decreasing temperature (Fig. 5), early-formed Fe-rich droplets will continue to exsolve elements that would preferentially partition into the Si-rich liquid [e.g., Fig. 1b of Charlier and Grove (2012)] such as those required to grow albitic plagioclase. At a plagioclase growth rate of 1.4×10^{-10} m/s (as calculated for an experimental charge quenched at 1010 °C; Table 3), a 3 μm pillar protruding from a crystal face would grow in ~ 6 h if the Fe-rich droplets were present from 1025 °C. This idea is compatible with the suggestion that the viscosity contrasts between the Fe-rich droplets and Si-rich liquid are large and that this affects the chemical diffusion of elements to the growing plagioclase (Philpotts 1981; see S. Table B). The Fe-rich droplet has a lower viscosity and so rapidly diffuses material to the growing plagioclase face in comparison with diffusion rates through the higher viscosity Si-rich liquid (Philpotts 1981).

Wetting angles

Are the wetting angles in textural equilibrium?

Wetting angles are a result of the balance of three interfacial energies and are therefore controlled by the compositions of the crystal substrate, the Fe-rich liquid, and the Si-rich liquid (e.g. Yablonovitch and Gmitter 1984). For the specific case of the Fe-rich droplets on plagioclase, this force balance is described by the Young equation: $\acute{y}_{PSi} - \acute{y}_{PFe} - \acute{y}_{SiFe} \cos\Theta = 0$, where P denotes plagioclase, Fe denotes the Fe-rich liquid forming the droplet, Si denotes the Si-rich liquid, and Θ denotes the wetting angle (Young 1805). Although we have little idea of the extent of anisotropy of the $\acute{y}_{Psi}$ and $\acute{y}_{PFe}$ interfacial energies, we might expect a single value (or narrow range) of the wetting angle if the system was in textural equilibrium, but a wide range of values if it was far from equilibrium. The presence of more than one value of wetting angle in a sample can be ascertained by comparison of the observed cumulative frequency curve for the 2D angle population with that calculated for a system with a single 3D angle value. If the sample contains a wide range of true 3D angles, the observed cumulative frequency curve will be broader and flatter than the theoretical curve (Elliott et al. 1997; Harker and Parker 1945; Riegger and Van Vlack 1960).

The population of apparent wetting angles is generally unimodal (S. Figure A), with similarities in distribution for experiments held isothermally for different durations (S. Figure A(b)). The bimodal distribution measured in the experiment quenched at 1030 °C may be attributed to the small measurement population ($n = 29$; Table 4). The cumulative frequency plots show rather narrower distributions than expected for single valued angles intersected in randomly

oriented 2D sections (Riegger and Van Vlack 1960: S. Figure B), consistent with the unlikelihood of observing droplets intersected at low angles in experiments containing a limited number of droplets and with a single value of wetting angle in 3D. We conclude therefore that the observed droplet morphology reflects textural equilibrium. This conclusion is supported by the results of Veksler et al. (2008), (2010), who suggested that Fe-rich droplets with diameters less than 12–14 μm equilibrated with the surrounding liquid on a timescale of several minutes.

Wetting angle variations

At the apex of the binodal, the compositional similarity of the two liquids means that the energy of the Fe-rich liquid–plagioclase interface should be equivalent to the Si-rich liquid–plagioclase interface: the wetting angle of the Fe-rich liquid (and that of the Si-rich liquid) on all mineral surfaces at the apex of the binodal should therefore be 90° (as observed, Fig. 6a). With decreasing temperature, the divergence of the compositions of the two liquids increases both the energy of the interface between the two liquids and the difference between the two liquid–plagioclase interfacial energies. The 30° down temperature increase in the wetting angle of Fe-rich liquid on plagioclase is controlled by the relative rates at which these interfacial energies change. There is more compositional similarity between the Si-rich liquid and plagioclase [particularly given the increasingly sodic plagioclase compositions at lower temperatures (S. Table B)], therefore we expect the energy of this interface to decrease with decreasing temperature, while that of both the Fe-rich liquid–plagioclase interface and the two-liquid interface increases. Since the wetting angle of the Fe-rich liquid increases from 90° with decreasing temperature, the dominant control on the wetting angle must be the difference between the two liquid–plagioclase interfacial energies.

The wetting angle of the Fe-rich liquid on magnetite is significantly lower than 90° (some 20 °C below the temperature at which unmixing starts), and increases (although only slightly) with decreasing temperature (Fig. 6a). Since the Fe-rich liquid and magnetite are compositionally similar, we might expect the energy of this interface to decrease with decreasing temperature, while that of both the Si-rich liquid–magnetite interface and the two-liquid interface increases. The slight increase in wetting angle of the Fe-rich liquid on magnetite with decreasing temperature must therefore be dominated by the increase in the two-liquid interfacial energy.

In experimental charges that underwent constant cooling, the proportion of isolated relative to attached droplet areas increases as wetting angles increase, for angles > 90° (Fig. 10a). The Mull experiments from Charlier and Grove (2012) have wetting angles < 90° and we would therefore expect attached droplets to dominate, yet isolated droplets dominate in the experiments quenched at temperatures > 1000 °C. We suggest this is due to: (1) the composition at which the Mull liquid line of descent intersects the binodal; (2) the shape of the Mull composition binodal [Fig. 2 of Charlier and Grove (2012)]; and (3) the extent of Fe-rich liquid accumulation [Fig. 1b of Charlier and Grove (2012)]. Furthermore, the relative volume of the two immiscible liquids may affect the effectiveness of the separation of the two phases (Sato and Sumita 2007). For the Mull composition, the liquid line of descent crosses the binodal at a central position, closer to the apex than in our Sept Iles composition experiments. Consequently, there is a greater volume of Fe-rich liquid at a given temperature, yet only a fixed crystal surface area on which droplets can sit (Fig. 12). At higher temperatures, where crystallinity is lower, this results in more isolated droplets. The Mull binodal is also a different shape to the Sept Iles binodal [Fig. 2 of Charlier and Grove (2012)]. Crystallinity increases down temperature, therefore the proportion of isolated Fe-rich droplets should simultaneously reduce. In Fig. 1b of Charlier and Grove (2012), it is evident that the experimental charges with a Mull starting composition contain large patches of Fe-rich glass, commensurate with the size of the adjacent crystal grains. These are far larger than the size of Fe-rich droplets in our Sept Iles composition experimental charges. In our experiments, the Fe-rich liquid accumulated in semi-enclosed regions, locally covering entire plagioclase faces, and thereby maintaining the area of Fe-rich glass in direct contact with plagioclase.

Droplet evolution

The evolution (and hence size) of a Fe-rich droplet can be controlled by a range of factors such as coalescence, and growth due either to chemical equilibration driven by the widening of the binodal during cooling, or by Ostwald ripening. Coalescence occurs as droplets collide, and is a function of droplet radius, viscosity, density and the energy of the interface (Yao et al. 2005). Closely adjacent droplets float on their combined interface until the thin layer of liquid between the two droplets drains out (Deka et al. 2019). Ostwald ripening in liquid emulsions is diffusion controlled and driven by differences in solubility related to differences of surface curvature. Coarsening via Ostwald ripening is described by either LSW theory (Lifshitz and Slyozov 1961; Wagner 1961), which assumes a particle's coarsening rate is independent of its surroundings, or by the "communicating neighbours" (CN) theory (DeHoff 1991), based on the idea that only particles in close proximity affect each other's evolution (Higgins 2002).
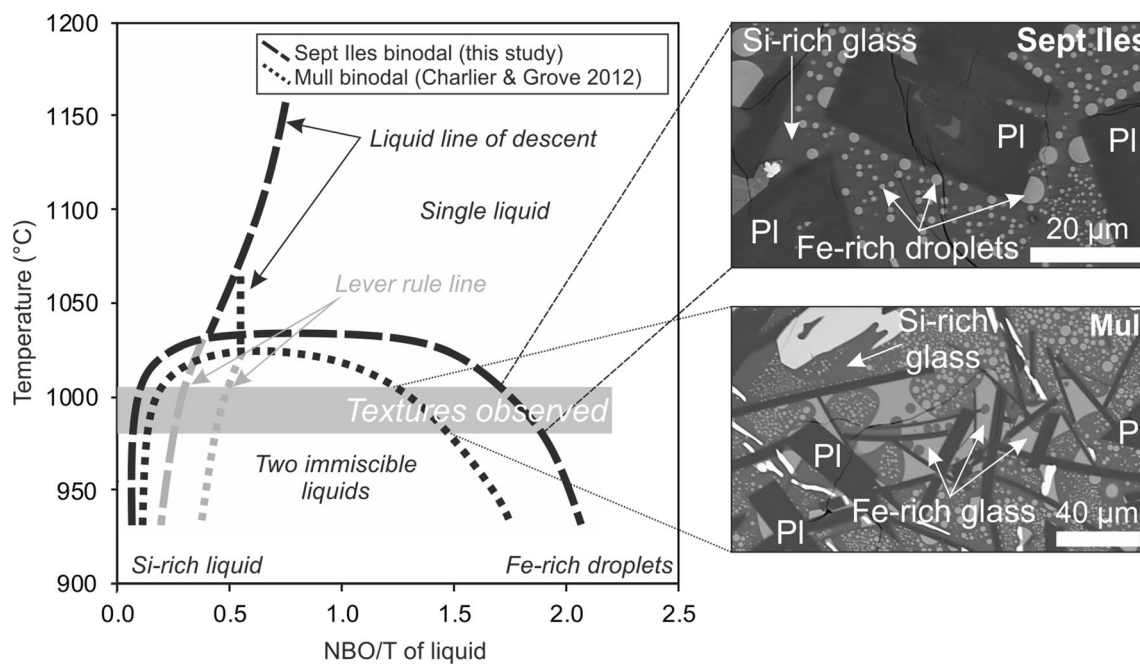
Fig. 12 Schematic illustration of the evolution of the liquid line of descent through a two-liquid field for a Sept Iles and Mull starting composition. Differing physical behaviour of the immiscible Fe-rich liquid is illustrated for each composition

Isothermal evolution

The Fe-rich droplets in our experiments held under isothermal conditions coarsen with time. For charges held isothermally at 1000 °C, the DSDs show that the d_{IS} is within bin size error of $d_{IS}*$ (Fig. 9d), consistent with some control by Ostwald ripening. Both coalescence and Ostwald ripening (using LSW theory) result in droplet mean diameters increasing with the cube root of time (Crist and Nesarikar 1995), but these two processes can be distinguished using the distribution of droplet sizes. Farr et al. (2017) calculated that Ostwald ripening leads to a ratio of volume-weighted mean droplet diameter versus the surface-weighted mean droplet diameter ($D_{4,3}/D_{3,2}$) of 1.0239, whereas coalescence is characterised by $D_{4,3}/D_{3,2} = 1.0748$. Farr et al. (2017) applied this model to an example of Fe-rich immiscible droplets in the experimental charges of Charlier and Grove (2012), finding a broader range of values (between 1.06 and 1.80) than predicted by either coalescence or Ostwald ripening. Similarly, our $D_{4,3}/D_{3,2}$ values for isolated droplets in our isothermal experiments (Table 5) lie between 1.09 and 1.54. This again suggests coarsening is controlled neither by Ostwald ripening alone nor by coalescence.

The timescale for coalescence is given by $\frac{\mu R}{\gamma}$, where μ is the dynamic viscosity of the more viscous liquid, R is the average radius of the two droplets, and γ is the interfacial tension between the two unmixed liquids (Paulsen et al. 2014; Rahman et al. 2019; Yao et al. 2005). Using the calculated viscosities in our experiments of 10^6 Pa.s (S. Table B), a radius of 0.8–4 μm (Table 5), and an estimated interfacial tension of 5–8 mN/m (Veksler et al. 2010), we predict coalescence on timescales of 160–800 s, sufficient to expect evidence of partial coalescence to be preserved in the quenched experimental runs. Over 27,000 Fe-rich droplets were analysed in this study, yet only two examples of partially complete coalescence (i.e. two droplets forming a 'figure of eight') were found, and only a few examples of two droplets in close proximity separated by a meniscus (Fig. 3). This suggests that coalescence was not a significant process controlling droplet size distribution in our experiments.

Instead, since droplet composition also evolves with dwell time (S. Table B), we suggest that coarsening is likely to have been controlled by a combination of kinetic growth and chemical equilibration as the binodal widened during cooling. A further possible cause of the loss of small droplets is the increasing difficulty in nucleation as the pockets of remaining liquid become smaller with increasing crystallinity (e.g. Putnis and Mauthe 2001).

Constant cooling evolution

While the compositional evolution of the isothermal experiments shows that these experiments did not reach chemical equilibrium, this is even more the case for the experiments which underwent constant cooling, in which chemical

equilibrium is a "constantly moving goalpost". The DSDs in the constantly cooled experimental charges are non-linear. In natural systems, such size distributions have been attributed to changes in cooling rate (Zieg and Marsh 2002), yet our experimental charges were run with a constant cooling rate of 1 °C/h. Such nonlinearity may be due to a combination of diffusion-controlled droplet growth (including Ostwald ripening), and nucleation (e.g. Cashman and Ferry 1988).

Coarsening during constant cooling increases both d_{IS} and d_{AT}. Our data show $D_{4,3}/D_{3,2}$ values for isolated droplets (Table 5) lie between 1.09 and 1.21 (with one exception—attributed to differences in experimental starting preparation). These ratios are broadly consistent with previous analysis of Fe-rich droplet size distributions in the experimental charges of Charlier and Grove (2012) by Farr et al. (2017) and, in common with the isothermal experimental results, suggests a significantly wider size distribution for isolated Fe-rich droplets than predicted if coarsening were exclusively by Ostwald ripening.

The DSDs show that the d_{IS} is within bin size error of the $d_{IS}*$. Furthermore, the DSDs have a positive slope for $d_{IS} < d_{IS}*$ (Fig. 8). These observations suggest Ostwald ripening played some role in coarsening (Cashman and Ferry 1988). The DSDs for isolated droplets rotate towards the horizontal (Fig. 8), compatible with the CN theory of Ostwald ripening (DeHoff 1991; Higgins 2002). This supports our idea of small-scale compositional heterogeneities influencing unmixing in localised areas within the crystal mush. However, a reduction in the number of small droplets could also result from a lowering of the nucleation rate (due perhaps to a reduction in the driving force for nucleation caused by decreased pore size). The DSDs for attached droplets do not show evidence of coarsening via Ostwald ripening.

Binodal position

The highest-temperature record of the onset of unmixing in semi-isolated pockets of skeletal plagioclase is in the experimental charge quenched at 1030 °C. The bulk interstitial liquid records the onset of immiscibility in the experimental charges quenched at 1025 °C and below, consistent with previous studies (Charlier and Grove 2012). For any given quench temperature, we observe a range of compositions of the co-existing Fe-rich and Si-rich liquids (Fig. 5). Previously published binodals were determined using the average of these compositions (B. Charlier pers. comm. 2018). Here we draw the binodal using the extreme values of our calculated NBO/T values (as discussed below).

There is a small disparity between the compositional ratio of Fe-rich/Si-rich liquids (obtained by applying the lever rule to the binodal) and the relative proportions of Fe-rich/Si-rich glass measured in the experimental charges. We attribute this disparity to the analytical limitations imposed

by EPMA spatial resolution, which prevented us from analysing smaller Fe-rich droplets. These analytical limitations also resulted in the observed range in Fe-rich droplet compositions within any one experimental charge, since the larger droplets are not necessarily compositionally comparable to the smaller, sub-micron, droplets. The large Fe-rich droplets are internally unmixed and heterogeneous, sometimes containing abundant nano-scale Si-rich droplets [shown in Fig. 1b of Charlier and Grove (2012)]. Consequently, we suggest that the large Fe-rich droplets have a less evolved composition than the smaller Fe-rich droplets. This suggestion is supported by changes in glass compositional analyses from the experimental charges as the isothermal dwell time increases. Since the Fe-rich droplets evolve to more Fe-rich compositions and higher NBO/T compositions (S. Table B) with increasing dwell time, we suggest that the Fe-rich end member of the binodal has a higher NBO/T value than our compositional analyses suggest. This would widen the binodal (Fig. 5), and hence reduce the calculated relative proportion of Fe-rich/Si-rich liquid, resulting in the measured liquid proportions more closely matching the binodal calculated proportions.

Furthermore, we do not know the exact compositional evolution of the bulk liquid line of descent. The bulk liquid NBO/T should first increase prior to magnetite saturation (Fe enrichment of tholeiitic trends). Then, the NBO/T decreases (Si enrichment) and this bulk Si enrichment continues even after the binodal is reached. Consequently, the bulk liquid line of descent gets closer to the Si-rich side of the binodal (Fig. 12) while the binodal simultaneously enlarges; it is therefore difficult to predict whether the volume of Fe-rich liquid should decrease or increase with cooling.

Increasing the isothermal dwell time of the experimental charges results in an apparent decrease in the volume of Fe-rich liquid. At first glance, this suggests the unmixed liquid has not attained chemical equilibrium; however, this is at odds with the extensively documented natural examples of emulsions in liquids of similar compositions to those of our experiments (e.g. De 1974; Luais 1987; Philpotts 1979; Philpotts and Philpotts 2005). We suggest that since our experimental charges continue to crystallise during isothermal equilibration, the continued evolution of the remaining liquid could result in the liquid line of descent exiting the binodal.

Implications for immiscible liquid separation

Our unmixing experiments focus on the evolution of silicate liquid immiscibility microstructures in tholeiitic systems in which the Fe-rich liquid is the minor phase, forming dispersed droplets within a continuous Si-rich phase, with results applicable to a wide array of tholeiitic systems. Previous studies

have hypothesised that large-scale phase separation can occur following unmixing of the bulk tholeiitic magma (Charlier et al. 2011; Jakobsen et al. 2011; Namur et al. 2012; VanTongeren and Mathez 2012). Gravitationally driven liquid separation in the bulk magma of such systems depends on the Stokes' velocity of the droplets, and would be least efficient close to the binodal, where liquid compositions are similar (Hou et al. 2017; Yuan et al. 2017). The Stokes' velocity of an Fe-rich droplet is given by: $v = \frac{2g\Delta pR^2}{9\eta}$. Using the known density (ρ), viscosity (η), and average isolated Fe-rich droplet radius (R) (S. Table B), settling velocities range from 10^{-8}–10^{-10} m/year. The maximum migration distance of an average Fe-rich droplet on the solidification timescales of 10 km-scale layered intrusions (e.g., ~ 100,000 to 1,000,000 years) is 10^{-2}–10^{-3} m. This falls well below the separation lengthscale of hundreds of metres suggested by VanTongeren and Mathez (2012) for the Upper Zone of the Bushveld Complex. Large-scale separation of liquid emulsions therefore requires either much larger droplet sizes, or processes such as convection which could facilitate the segregation of the two immiscible liquids if the dense component of the convecting emulsion were retained on the floor and the light component at the roof. While this may be the case for magmas in which the Fe-rich liquid comprises significantly less than 50 vol.%, at higher volume fractions centrifuge experiments show that the Fe-rich droplets may form 'avalanches' to facilitate separation (Veksler et al. 2008): it is therefore possible that Stokes' law may not apply under such compositional conditions. Additionally, Veksler et al. (2008) showed that gravitationally driven separation of a nano-emulsion is possible in both a centrifuge and under static experimental conditions, so treatments of unmixing timescales based on Stokes' law may be unrealistic.

Separation of immiscible liquids within a crystal mush (e.g. Holness et al. 2011; Humphreys 2009, 2011) is strongly affected by pore diameters, coarsening rates and wetting properties. For example, Chung and Mungall (2009) show that immiscible sulphide droplets with radii $\frac{1}{10}$ the average crystal radius travel the furthest through a crystal mush. Plagioclase comprises over 68% of the solid phases in our experiments; the average plagioclase grain is 22.8 μm along the major axis (Table 3), so Fe-rich droplets of radius 4.8 μm might be expected to be the most mobile. This is an order of magnitude larger than the average diameter of homogeneously nucleated droplets in our experiments (Table 5), so optimal segregation of the two immiscible phases in a crystal mush of equivalent grain size requires significant droplet coarsening (ignoring the effect of pore throat dimension). Consequently, in small-scale, crystal-rich tholeiitic magma bodies cooling on the order of 1 °C/h (e.g. dykes and sills of ~ 10 m width), gravitationally driven segregation of immiscible homogeneously nucleated Fe-rich droplets is unlikely to be significant. Chung and Mungall (2009)

suggest that if the dense immiscible liquid forms a connected net-like texture around crystals (i.e. the dense liquid phase wets the minerals of the mush), this can promote phase separation. Consequently, coarsening and accumulation of pockets of Fe-rich liquid should better facilitate downwards movement in a mush, relative to dispersed isolated droplets. This is most likely to pertain to mushes, or regions of mushes, rich in phases on which the Fe-rich liquid has a low wetting angle, such as oxides and mafic minerals like olivine and pyroxene (Table 4). This effect may be promoted by the presence of water, which enlarges the binodal surface and increases the interfacial tension between the two immiscible liquids (Hou et al. 2018), making coalescence more effective compared to dry tholeiitic systems. The concentration of the elements Ca, Al and Si also has an effect on coarsening rates, with unmixing shown to be significantly slowed by high concentrations of these elements regardless of temperature (Veksler et al. 2008). A further factor controlling segregation is that the closer the liquid line of descent is to the centre of the binodal, the greater the volume of Fe-rich liquid at higher temperatures, promoting Fe-rich liquid migration.

Concluding remarks

The results of this experimental study illustrate how thermal history and crystallisation affect the physical behaviour of an immiscible Fe-rich liquid during cooling of a ferrobasaltic liquid. The key findings are:

1. The onset of unmixing is localised because of heterogeneities in the interstitial liquid produced by compositional boundary layers formed during crystallisation;
2. Accumulations of small grains of whitlockite (similar to apatite in composition) along the margins of pyroxene and magnetite grains, and albitic pillars on plagioclase grains, provide potential microstructural indicators of immiscibility in fully solidified rocks;
3. The wetting angles of Fe-rich immiscible liquids on plagioclase and magnetite increase with decreasing temperature;
4. Heterogeneously nucleated droplets do not coarsen solely via Ostwald ripening during the experiments;
5. Droplet size distributions of homogeneously nucleated droplets are controlled strongly by growth during the process of chemical equilibration driven by cooling, with minimal contribution from coalescence;
6. In small-scale magma bodies (e.g. dykes and sills of ~ 10 m width), gravitationally driven segregation of immiscible homogeneously nucleated Fe-rich droplets is unlikely to be significant.

Although the cooling rates of our experiments were analogous to those experienced by a small intrusion, further work at lower cooling rates would provide microstructural evidence applicable to larger bodies.

References

Anderson A, Greenland L (1969) Phosphorus fractionation diagram as a quantitative indicator of crystallization differentiation of basaltic liquids. Geochim Cosmochim Acta 33:493–505

Bogaerts M, Schmidt M (2006) Experiments on silicate melt immiscibility in the system Fe2SiO4–KAlSi3O8–SiO2–CaO–MgO–TiO2–P2O5 and implications for natural magmas. Contrib Miner Petrol 152:257–274

Boorman S, Boudreau A, Kruger F (2004) The Lower Zone-Critical Zone transition of the Bushveld Complex: a quantitative textural study. J Petrol 45:1209–1235

Bottinga Y, Weill DF (1970) Densities of liquid silicate systems calculated from partial molar volumes of oxide components. Am J Sci 269:169–182

Brunet F, Chazot G (2001) Partitioning of phosphorus between olivine, clinopyroxene and silicate glass in a spinel lherzolite xenolith from Yemen. Chem Geol 176:51–72. https://doi.org/10.1016/S0009-2541(00)00351-X

Cahn JW (1961) On spinodal decomposition. Acta metallurgica 9:795–801

Cashman KV, Ferry JM (1988) Crystal size distribution (CSD) in rocks and the kinetics and dynamics of crystallization. Contrib Miner Petrol 99:401–415. https://doi.org/10.1007/bf00371933

Charlier B, Grove TL (2012) Experiments on liquid immiscibility along tholeiitic liquid lines of descent. Contrib Miner Petrol 164:27–44

Charlier B, Namur O, Toplis MJ, Schiano P, Cluzel N, Higgins MD, Vander Auwera J (2011) Large-scale silicate liquid immiscibility during differentiation of tholeiitic basalt to granite and the origin of the Daly gap. Geology 39:907–910

Chen Y, Zhang Y (2008) Olivine dissolution in basaltic melt. Geochim Cosmochim Acta 72:4756–4777

Chen Y, Zhang Y (2009) Clinopyroxene dissolution in basaltic melt. Geochim Cosmochim Acta 73:5730–5747. https://doi.org/10.1016/j.gca.2009.06.016

Chung H-Y, Mungall JE (2009) Physical constraints on the migration of immiscible fluids through partially molten silicates, with special reference to magmatic sulfide ores. Earth Planet Sci Lett 286:14–22

Crist B, Nesarikar AR (1995) Coarsening in polyethylene-copolymer blends. Macromolecules 28:890–896

De A (1974) Silicate liquid immiscibility in the Deccan Traps and its petrogenetic significance. Geol Soc Am Bull 85:471–474

DeHoff RT (1991) A geometrically general theory of diffusion controlled coarsening. Acta Metall Mater 39:2349–2360. https://doi.org/10.1016/0956-7151(91)90016-T

Deka H, Biswas G, Chakraborty S, Dalal A (2019) Coalescence dynamics of unequal sized drops. Phys Fluids 31:012105

Dixon S, Rutherford M (1979) Plagiogranites as late-stage immiscible liquids in ophiolite and mid-ocean ridge suites: an experimental study. Earth Planet Sci Lett 45:45–60

Drouin D, Réal Couture A, Joly D, Tastet X, Aimez V, Gauvin R (2007) CASINO V2.42—a fast and easy-to-use modeling tool for scanning electron microscopy and microanalysis users. Scanning 29(3):92–101. https://doi.org/10.1002/sca.20000

Dufek J (2016) Multiphase flow in crustal magmatic processes. In: Melt in the mantle: from foundations to state-of-the-art in magma/mantle dynamics. Isaac Newton Institute for Mathematical Sciences, Cambridge

Dunbar NW, Jacobs GK, Naney MT (1995) Crystallization processes in an artificial magma: variations in crystal shape, growth rate and composition with melt cooling history. Contrib Miner Petrol 120:412–425. https://doi.org/10.1007/bf00306518

Elliott CM (1989) The Cahn-Hilliard model for the kinetics of phase separation. In: Rodrigues JF (ed) Mathematical models for phase change problems. Springer, pp 35–73

Elliott MT, Cheadle MJ, Jerram DA (1997) On the identification of textural equilibrium in rocks using dihedral angle measurements. Geology 25:355–358

Farr RS, Honour VC, Holness MB (2017) Mean grain diameters from thin sections: matching the average to the problem. Mineral Mag 81:515–530

Fischer LA et al (2016) Immiscible iron- and silica-rich liquids in the Upper Zone of the Bushveld Complex. Earth Planet Sci Lett 443:108–117. https://doi.org/10.1016/j.epsl.2016.03.016

German RM, Suri P, Park SJ (2009) Liquid phase sintering. J Mat Sci 44(1):1–39

Giordano D, Russell JK, Dingwell DB (2008) Viscosity of magmatic liquids: a model. Earth Planet Sci Lett 271:123–134. https://doi.org/10.1016/j.epsl.2008.03.038

Grove TL (1982) Use of FePt alloys to eliminate the iron loss problem in 1 atmosphere gas mixing experiments: theoretical and practical considerations. Contrib Mineral Petrol 78(3):298–304

Hammer JE, Sharp TG, Wessel P (2010) Heterogeneous nucleation and epitaxial crystal growth of magmatic minerals. Geology 38:367–370. https://doi.org/10.1130/g30601.1

Harker D, Parker ER (1945) Grain shape and grain growth. Trans Am Soc Met 34:156–201

Hassanizadeh SM (2016) Advanced theories of two-phase flow in deformable porous media, including fluid-fluid interfaces. In: Melt in the mantle: from foundations to state-of-the-art in magma/mantle dynamics. Isaac Newton Institute for Mathematical Sciences, Cambridge

Helz R (1980) Crystallization history of Kilauea Iki lava lake as seen in drill core recovered in 1967–1979. Bull Volcanol 43:675–701

Helz RT, Wright TL (1992) Differentiation and magma mixing on Kilauea's east rift zone. Bull Volcanol 54:361–384

Higgins M (1994) Determination of crystal morphology and size from bulk measurements on thin sections: numerical modelling. Am Miner 79:113–119

Higgins MD (2000) Measurement of crystal size distributions. Am Miner 85:1105–1116

Higgins MD (2002) A crystal size-distribution study of the Kiglapait layered mafic intrusion, Labrador, Canada: evidence for textural coarsening. Contrib Miner Petrol 144:314–330

Holness MB (2006) Melt-solid dihedral angles of common minerals in natural rocks. J Petrol 47:791–800. https://doi.org/10.1093/petrology/egi094

Holness MB (2014) The effect of crystallization time on plagioclase grain shape in dolerites. Contrib Miner Petrol 168:1076

Holness MB, Sawyer EW (2008) On the pseudomorphing of melt-filled pores during the crystallization of migmatites. J Petrol 49:1343–1363

Holness MB, Stripp G, Humphreys M, Veksler IV, Nielsen TF, Tegner C (2011) Silicate liquid immiscibility within the crystal mush: late-stage magmatic microstructures in the Skaergaard intrusion, East Greenland. J Petrol 52:175–222

Holness MB, Neufeld JA, Gilbert AJ, Macdonald R (2017) Orientation of tabular mafic intrusions controls convective vigour and crystallization style. J Petrol 58:2035–2053. https://doi.org/10.1093/petrology/egx081

Hou T, Veksler IV (2015) Letter. Experimental confirmation of high-temperature silicate liquid immiscibility in multicomponent ferrobasaltic systems. Am Miner 100:1304–1307

Hou T, Charlier B, Namur O, Schütte P, Schwarz-Schampera U, Zhang Z, Holtz F (2017) Experimental study of liquid immiscibility in the Kiruna-type Vergenoeg iron–fluorine deposit, South Africa. Geochim Cosmochim Acta 203:303–322

Hou T, Charlier B, Holtz F, Veksler I, Zhang Z, Thomas R, Namur O (2018) Immiscible hydrous Fe–Ca–P melt and the origin of iron oxide-apatite ore deposits. Nat Commun 9:1415. https://doi.org/10.1038/s41467-018-03761-4

Humphreys MC (2009) Chemical evolution of intercumulus liquid, as recorded in plagioclase overgrowth rims from the Skaergaard intrusion. J Petrol 50:127–145

Humphreys MC (2011) Silicate liquid immiscibility within the crystal mush: evidence from Ti in plagioclase from the Skaergaard intrusion. J Petrol 52:147–174

Jakobsen JK, Veksler I, Tegner C, Brooks CK (2005) Immiscible iron- and silica-rich melts in basalt petrogenesis documented in the Skaergaard intrusion. Geology 33:885–888

Jakobsen JK, Veksler IV, Tegner C, Brooks CK (2011) Crystallization of the Skaergaard intrusion from an emulsion of immiscible iron- and silica-rich liquids: evidence from melt inclusions in plagioclase. J Petrol 52(2):345–373

Kouchi A, Sugawara Y, Kashima K, Sunagawa I (1983) Laboratory growth of sector zoned clinopyroxenes in the system CaMgSi2O6-CaTiAl2O6. Contrib Miner Petrol 83:177–184. https://doi.org/10.1007/bf00373091

Lifshitz IM, Slyozov VV (1961) The kinetics of precipitation from supersaturated solid solutions. J Phys Chem Solids 19:35–50

Lofgren GE (1983) Effect of heterogeneous nucleation on basaltic textures: a dynamic crystallization study. J Petrol 24:229–255

Longhi J (1990) Silicate liquid immiscibility in isothermal crystallization experiments. In: Lunar and Planetary Science Conference Proceedings, 20th, Houston, TX, Mar. 13-17, 1989, ouston, TX, Lunar andPlanetary Institute, pp 13–24

Luais B (1987) Immiscibilité entre liquides silicatés dans les mésostases et les inclusions vitreuses des andésites basiques de Santorin (Arc Egéen). Bull Minér 110:93–109

Lundstrom C, Boudreau A, Pertermann M (2005) Diffusion–reaction in a thermal gradient: Implications for the genesis of anorthitic plagioclase, high alumina basalt and igneous mineral layering. Earth Planet Sci Lett 237:829–854

Marsh BD (1988) Crystal size distribution (CSD) in rocks and the kinetics and dynamics of crystallization. Contrib Miner Petrol 99:277–291. https://doi.org/10.1007/bf00375362

Martin B, Kushiro I (1991) Immiscibility synthesis as an indication of cooling rates of basalts. J Volcanol Geoth Res 45:289–310

Morse SA, Brady JB (2017) Thermal History of the Upper Zone of the Kiglapait Intrusion. J Petrol 58:1319–1332. https://doi.org/10.1093/petrology/egx055

Mullis AM (2003) A study of kinetically limited dendritic growth at high undercooling using phase-field techniques. Acta Mater 51:1959–1969. https://doi.org/10.1016/S1359-6454(02)00601-8

Mungall JE, Su S (2005) Interfacial tension between magmatic sulfide and silicate liquids: Constraints on kinetics of sulfide liquation and sulfide migration through silicate rocks. Earth Planet Sci Lett 234:135–149. https://doi.org/10.1016/j.epsl.2005.02.035

Mysen BO (1983) The structure of silicate melts. Annu Rev Earth Planet Sci 11:75–97

Namur O, Charlier B, Toplis MJ, Higgins MD, Hounsell V, Liégeois J-P, Vander Auwera J (2011) Differentiation of tholeiitic basalt to A-type granite in the Sept Iles layered intrusion, Canada. J Petrol 52:487–539

Namur O, Charlier B, Holness MB (2012) Dual origin of Fe–Ti–P gabbros by immiscibility and fractional crystallization of evolved tholeiitic basalts in the Sept Iles layered intrusion. Lithos 154:100–114

Naslund H (1976) Liquid immiscibility in the system KAlSi3O8-NaAlSi3O8-FeO-Fe2O3-SiO2 and its application to natural magmas. Carnegie Inst Wash 75:592–597

Neave DA, Buisman I, Maclennan J (2017) Continuous mush disaggregation during the long-lasting Laki fissure eruption, Iceland. Am Miner 102:2007–2021. https://doi.org/10.2138/am-2017-6015ccby

Paulsen JD, Carmigniani R, Kannan A, Burton JC, Nagel SR (2014) Coalescence of bubbles and drops in an outer fluid. Nat Commun 5:3182. https://doi.org/10.1038/ncomms4182

Philpotts A (1977) Archean variolites—quenched immiscible liquids: Discussion. Can J Earth Sci 14:139–144

Philpotts AR (1979) Silicate liquid immiscibility in tholeiitic basalts. J Petrol 20:99–118

Philpotts AR (1981) A model for the generation of massif-type anorthosites. Can Miner 19:233–253

Philpotts A (1982) Compositions of immiscible liquids in volcanic rocks. Contrib Miner Petrol 80:201–218

Philpotts A, Doyle C (1980) Immiscibility in tholeiites: a discussion. Miner Mag 43:939–940

Philpotts AR, Doyle CD (1983) Effect of magma oxidation state on the extent of silicate liquid immiscibility in a tholeiitic basalt. Am J Sci 283:967–986. https://doi.org/10.2475/ajs.283.9.967

Philpotts AR, Philpotts DE (2005) Crystal-mush compaction in the Cohasset flood-basalt flow, Hanford, Washington. J Volcanol Geoth Res 145:192–206

Pleše P et al (2018) Dynamic observations of vesiculation reveal the role of silicate crystals in bubble nucleation and growth in andesitic magmas. Lithos 296–299:532–546. https://doi.org/10.1016/j.lithos.2017.11.024

Putnis A, Mauthe G (2001) The effect of pore size on cementation in porous rocks. Geofluids 1:37–41. https://doi.org/10.1046/j.1468-8123.2001.11001.x

Rahman MM, Lee W, Iyer A, Williams SJ (2019) Viscous resistance in drop coalescence. Phys Fluids 31:012104

Riegger O, Van Vlack L (1960) Dihedral angle measurement. Trans Metall Soc AIME 218:933–935

Roedder E, Weiblen PW (1970) Silicate liquid immiscibility in lunar magmas, evidenced by melt inclusions in lunar rocks. Science 167:641–644

Rotenberg Y, Boruvka L, Neumann AW (1983) Determination of surface tension and contact angle from the shapes of axisymmetric

fluid interfaces. J Colloid Interface Sci 93:169–183. https://doi.org/10.1016/0021-9797(83)90396-X

Sato H (1995) Textural difference between pahoehoe and aa lavas of Izu-Oshima volcano, Japan–An experimental study on population density of plagioclase. J Volcanol Geoth Res 66:101–114

Sato M, Sumita I (2007) Experiments on gravitational phase separation of binary immiscible fluids. J Fluid Mech 591:289–319

Stickels C, Hucke E (1964) Measurement of dihedral angles. Trans Metall Soc AIME 230:795–801

Tollari N, Toplis M, Barnes S-J (2006) Predicting phosphate saturation in silicate magmas: an experimental study of the effects of melt composition and temperature. Geochim Cosmochim Acta 70:1518–1536

VanTongeren J, Mathez E (2012) Large-scale liquid immiscibility at the top of the Bushveld Complex, South Africa. Geology 40:491–494

Veksler IV, Dorfman AM, Danyushevsky LV, Jakobsen JK, Dingwell DB (2006) Immiscible silicate liquid partition coefficients: implications for crystal-melt element partitioning and basalt petrogenesis. Contrib Miner Petrol 152:685–702

Veksler IV, Dorfman AM, Rhede D, Wirth R, Borisov AA, Dingwell DB (2008) Liquid unmixing kinetics and the extent of immiscibility in the system K2O–CaO–FeO–Al2O3–SiO2. Chem Geol 256:119–130

Veksler IV, Kähn J, Franz G, Dingwell DB (2010) Interfacial tension between immiscible liquids in the system K2O-FeO-Fe2O3-Al2O3-SiO2 and implications for the kinetics of silicate melt unmixing. Am Miner 95:1679–1685

Visser W, Koster Van Groos AF (1976) Liquid immiscibility in K2O–FeO–Al2O3–SiO2. Nature 264:426–427

Visser W, Van Groos AK (1979) Effects of P2O5 and TiO2 on liquid-liquid equilibria in the system K2O-FeO-Al2O3-SiO2. Am J Sci 279:970–988

Vukmanovic Z, Holness MB, Monks K, Andersen J (2018) The Skaergaard trough layering: sedimentation in a convecting magma chamber. Contrib Miner Petrol 173:1–18

Wagner C (1961) Theorie der alterung von niederschlägen durch umlösen (Ostwald-reifung). Zeitschrift für Elektrochemie, Berichte der Bunsengesellschaft für physikalische Chemie 65:581–591

Whitney DL, Evans BW (2010) Abbreviations for names of rock-forming minerals. Am Miner 95:185–187. https://doi.org/10.2138/am.2010.3371

Wilks S (1962) Mathematical statistics. Wiley, New York

Yablonovitch E, Gmitter T (1984) Wetting angles and surface tension in the crystallization of thin liquid films. J Electrochem Soc 131:2625–2630. https://doi.org/10.1149/1.2115372

Yao W, Maris H, Pennington P, Seidel G (2005) Coalescence of viscous liquid drops. Phys Rev E 71:016309

Young T (1805) III. An essay on the cohesion of fluids. Philos Trans R Soc Lond 95:65–87

Yuan Q, Namur O, Fischer LA, Roberts RJ, Lü X, Charlier B (2017) Pulses of plagioclase-laden magmas and stratigraphic evolution in the Upper Zone of the Bushveld Complex, South Africa. J Petrol 58:1619–1643

Zellmer GF, Sakamoto N, Hwang S-L, Matsuda N, Iizuka Y, Moebis A, Yurimoto H (2016) Inferring the effects of compositional boundary layers on crystal nucleation, growth textures, and mineral chemistry in natural volcanic tephras through submicron-resolution imaging. Front Earth Sci 4:88. https://doi.org/10.3389/feart.2016.00088

Zhou M-F, Chen WT, Wang CY, Prevec SA, Liu Patricia P, Howarth GH (2013) Two stages of immiscible liquid separation in the formation of Panzhihua-type Fe-Ti-V oxide deposits, SW China. Geosci Front 4:481–502. https://doi.org/10.1016/j.gsf.2013.04.006

Zieg M, Marsh B (2002) Crystal size distributions and scaling laws in the quantification of igneous textures. J Petrol 43:85–101